

# Multi-Dimensional Visual Data Recovery: Scale-Aware Tensor Modeling and Accelerated Randomized Computation

Wenjin Qin, Hailin Wang, Jiangjun Peng, Jianjun Wang, *Member, IEEE*, and Tingwen Huang, *Fellow, IEEE*

**Abstract**—The recently proposed *fully-connected tensor network* (FCTN) decomposition has demonstrated significant advantages in correlation characterization and transpositional invariance, and has achieved notable achievements in multi-dimensional data processing and analysis. However, existing multi-dimensional data recovery methods leveraging FCTN decomposition still have room for further enhancement, particularly in computational efficiency and modeling capability. To address these issues, we first propose a FCTN-based generalized nonconvex regularization paradigm from the perspective of gradient mapping. Then, reliable and scalable multi-dimensional data recovery models are investigated, where the model formulation is shifted from unquantized observations to coarse-grained quantized observations. Based on the *alternating direction method of multipliers* (ADMM) framework, we derive efficient optimization algorithms with convergence guarantees to solve the formulated models. To alleviate the computational bottleneck encountered when processing large-scale multi-dimensional data, fast and efficient randomized compression algorithms are devised in virtue of sketching techniques in numerical linear algebra. These dimensionality-reduction techniques serve as the computational acceleration core of our proposed algorithm framework. Theoretical results on approximation error upper bounds and convergence analysis for the proposed method are derived. Extensive numerical experiments illustrate the effectiveness and superiority of the proposed algorithm over other state-of-the-art methods in terms of quantitative metrics, visual quality, and running time.

**Index Terms**—Tensor network decomposition, high-order tensor recovery, multi-dimensional images restoration, randomized sketching technology, nonconvex gradient-domain regularization, global low-rankness and local smoothness

## I. INTRODUCTION

With the tremendous advancement of sensorial and information technology, multi-dimensional visual data have emerged widely in numerous modern application fields, including statistics [1], [2], biomedical imaging [3], [4], remote sensing [5]–[7], image and video processing [8], [9],

This work was supported in part by the National Key Research and Development Program of China under Grant 2023YFA1008502; in part by the National Natural Science Foundation of China under Grant U24A2001, in part by the Natural Science Foundation of Chongqing, China, under Grant CSTB2023NSCQ-LZX0044; and in part by Chongqing Talent Project, China, under Grant csc2021ycjh-bgzx0015. (Corresponding author: Jianjun Wang.)

Wenjin Qin and Jianjun Wang are with the School of Mathematics and Statistics, Southwest University, Chongqing 400715, China (e-mail: qinwenjin2021@163.com, wjj@swu.edu.cn).

Hailin Wang is with the Department of Statistics and Data Science, The Chinese University of Hong Kong, Shatin, Hong Kong (e-mail: wanghailin97@163.com).

Jiangjun Peng is with the School of Mathematics and Statistics, Northwestern Polytechnical University, Xi'an 710021, China (e-mail: pengjj@nwpu.edu.cn).

Tingwen Huang is with the Faculty of Computer Science and Control Engineering, Shenzhen University of Advanced Technology, Shenzhen 518055, China (e-mail: huangtingwen2013@gmail.com).

and computer vision [10], [11]. These data typically exhibit high dimensionality, multiple modalities, large volume, high veracity, and complex structure, thereby posing substantial challenges to subsequent relevant processing and analysis tasks [12]–[14]. For instance, large volume demands scalable strategies that can adapt to increasing data scales; high veracity calls for robust and reliable methods for noisy, incomplete and/or inconsistent data; and high dimensionality requires efficient compression techniques to mitigate the curse of dimensionality. As such, developing efficient and scalable multi-dimensional data processing/analysis approaches that can jointly address these challenges has become increasingly urgent and crucial.

Tensors (also known as multi-dimensional arrays), as the higher-order generalization of vectors and matrices, possess powerful capabilities in capturing the intrinsic structural characteristics embedded within a wide range of high-dimensional data. This advantage has driven the development of extensive tensor-based methodologies and theoretical frameworks, which are tailored for high-dimensional data processing and analysis [15], [16]. Among them, multi-dimensional data recovery is the most fundamental and crucial task, which addresses the challenge of reconstructing the clean data from its imperfect counterpart degraded by noise pollution, information missing, outliers interference, and other factors. Based on the solutions and techniques employed, existing tensor approaches for high-dimensional data recovery can be subdivided into two branches. The first branch is tensor factorization-based methods, which alternatively update the low-dimensional factors with the predefined initial tensor rank [17]–[23]. While demonstrating computational efficiency in certain scenarios, their performance heavily relies on accurate rank estimation. The other important branch is tensor regularization-based methods, whose idea is to characterize prior features (e.g., low-rankness, smoothness, sparsity) underlying multi-dimensional data finely via proper regularization items [24]–[36].

The *Tensor Nuclear Norm* (TNN) serves as a benchmark regularization paradigm, effectively inducing low-rank structure in high-dimensional data modeling. Within diverse tensor decomposition frameworks, researchers have extensively explored TNN-based regularization approaches for high-dimensional data recovery, accompanied by rigorous theoretical guarantees on exact recovery. Some typical examples include SNN [24] under Tucker framework, TTNN [33] under *tensor train* (TT) framework, TRNN [34], [35] under *tensor ring* (TR) framework, FCTN nuclear norm [21] under *Fully-Connected Tensor Network* (FCTN) framework, and HTNN [8], WSTNN [28], OITNN [29], METNN [31] under *Tensor*

*Singular Value Decomposition* (T-SVD) framework. To further enhance the recovery performance, a series of nonconvex variants with stronger low-rankness promoting capabilities have been successively proposed [6], [9], [32], [37]–[47]. Another influential regularization paradigm, *Tensor Correlated Total Variation* (TCTV), is essentially a tensor nuclear norm imposed on the gradient domain [10]. This method has been widely recognized for its ability to simultaneously constrain the low-rankness and smoothness of multi-dimensional data, see [10] and its extensions [48]–[50].

Although the above tensor regularization-based methods yield commendable performance in practical applications, they demonstrate inefficiency in handling large-scale multi-dimensional data. In response to the demands arising from the “V” features of the big data era, namely large Volume, high Velocity and high Veracity, it is of crucial importance to address the issue of large-scale multi-dimensional data recovery in a fast and accurate manner. Speed is manifested in the computation module, whereas accuracy is embodied in the modeling module. However, achieving high accuracy and fast speed simultaneously remains fraught with some challenges, because there is a trade-off between accuracy and speed.

### A. Our Motivations

Compared with the TT and TR decompositions, the FCTN decomposition adequately characterizes the correlations between any modes of the tensor, and avoids the influence of the permutations and the ordering of the tensor dimensions, thus showing outstanding performance on multi-dimensional data modeling [20], [21], [51]–[57]. However, existing multi-dimensional data recovery methods [20], [21], [51]–[56] leveraging FCTN decomposition still have room for further enhancement, particularly in modeling capability and computational efficiency.

1) *Modeling perspective*: In many application scenarios, the multi-dimensional visual data tend to exhibit strong global low-rankness (**L**) due to redundancy, and great local smoothness (**S**) due to fine-grained continuity. However, existing FCTN-based tensor regularization methods often failed to simultaneously capture these hybrid **L+S** characteristics in a concise yet effective manner. Besides, previous related models are limited to unquantized observations and are blind to the fact that real-world applications typically involve quantization of the data [20], [21], [51]–[56]. For some machine learning or signal/image processing systems involving large-scale tensors, it would be impractical to work with original tensor with high precision due to the prohibitive storage requirements, communication bandwidth limitations or excessive power consumption [58]–[60]. In this situation, a coarse-grained quantization method using a small number of bit-widths is more appropriate. *Therefore, we consider investigating concise yet effective FCTN-based tensor regularization strategies to reveal the insightful prior features of large-scale multi-dimensional data. This scheme takes into account the impact of data scale variations on its structural characteristics. Furthermore, reliable and scalable models for robust multi-dimensional data recovery are developed, where the model formulation is shifted*

*from unquantized to coarsely quantized observations. This is the first research motivation of this paper.*

2) *Computational perspective*: From a computational perspective, connecting any two factors in FCTN decomposition is a double-edged sword: the upside is that FCTN factorization provides a more flexible and superior representation compared to other decompositions; the downside is that FCTN decomposition encounters a high computational burden when dealing with large-scale multi-dimensional data, thereby incurring significant expenses for the associated tensor modeling methods [20], [21], [51]–[56]. This is because they generally experience the calculation of multiple SVDs of large-sized unfolding matrices or multiple large-sized *alternate least squares* (ALS) problems. Recently, randomized sketching techniques have been extensively investigated and have achieved great success in large-scale data analysis, especially in matrix/tensor approximation [57], [61]–[63]. The strength of randomized algorithms lies in their excellent computational efficiency, coupled with low memory storage requirements. Furthermore, their core operations can be optimized for maximum efficiency on modern computational platforms. *Therefore, we consider developing novel fast and accurate compression algorithms for large-scale high-order tensors in virtue of randomized sketching techniques, which maintain a low computational complexity while achieving an acceptable accuracy. These strategies aimed at dimensionality-reduction serve as the fundamental computational acceleration component in the design of our multi-dimensional data recovery algorithms. This is the second research motivation of this paper.*

### B. Our Contributions

1) In virtue of randomized sketching techniques in numerical linear algebra, we first devise fast and accurate randomized algorithms for large-scale high-order tensor compression. Additionally, theoretical results on error upper bounds for the proposed randomized algorithms are derived. Compared to existing compression approaches, the proposed method exhibits notable advantages in computational efficiency.

2) We propose an innovative nonconvex gradient-domain regularizer under FCTN decomposition framework, which simultaneously encodes both global low-rankness and local continuity of large-scale tensors. By combining it with another enhanced nonconvex noise/outlier regularization, novel robust multi-dimensional data recovery models are established, which cover a range from non-quantized to quantized observations.

3) To efficiently solve the proposed multiple recovery models, we develop efficient ADMM-based algorithms and theoretically demonstrate their convergence. Besides, to alleviate the computational burden faced by the proposed algorithms when processing large-scale multi-dimensional data, we technically embed the proposed randomized compression modules into its time-intensive optimization procedure.

4) Extensive experiments conducted on color images/videos, hyperspectral images/videos, magnetic resonance images, and face databases provide empirical support for the theoretical analysis, and demonstrate that the proposed method outperforms other state-of-the-art approaches quantitatively and

qualitatively. Strikingly, in cases of slight or no accuracy loss, our method incorporated randomized techniques decreases the CPU time by approximately 88% in comparison to the deterministic version (please refer to the experimental section for details).

## II. NOTATIONS AND PRELIMINARIES

In this section, we summarize the critical notations and preliminaries utilized in this paper.

1) **Notations:** We use  $x$ ,  $\mathbf{x}$ ,  $\mathbf{X}$ , and  $\mathcal{X}$  to denote scalars, vectors, matrices, and tensors, respectively. For simplicity, we use  $\mathbf{x}_{1:q}$ ,  $\mathbf{X}_{1:q}$ , and  $\mathcal{X}_{1:q}$  to represent ordered sets  $\{\mathbf{x}_1, \dots, \mathbf{x}_q\}$ ,  $\{\mathbf{X}_1, \dots, \mathbf{X}_q\}$ , and  $\{\mathcal{X}_1, \dots, \mathcal{X}_q\}$ , respectively. For tensor  $\mathcal{X} \in \mathbb{R}^{I_1 \times I_2 \times \dots \times I_N}$ , we denote  $\mathcal{X}_{i_1, i_2, \dots, i_N}$  as its  $(i_1, i_2, \dots, i_N)$ -th element. The **inner product** of two tensors  $\mathcal{X}$  and  $\mathcal{Y}$  with the same size is defined as the sum of the products of their entries, i.e.,  $\langle \mathcal{X}, \mathcal{Y} \rangle = \sum_{i_1, i_2, \dots, i_N} \mathcal{X}_{i_1, i_2, \dots, i_N} \cdot \mathcal{Y}_{i_1, i_2, \dots, i_N}$ . The  **$l_1$ -norm**, **Frobenius norm** and  **$l_{F,1}$ -norm** of  $\mathcal{X}$  are defined as  $\|\mathcal{X}\|_1 = \sum_{i_1, i_2, \dots, i_N} |\mathcal{X}_{i_1, i_2, \dots, i_N}|$ ,  $\|\mathcal{X}\|_F = \sqrt{\sum_{i_1, i_2, \dots, i_N} |\mathcal{X}_{i_1, i_2, \dots, i_N}|^2}$  and  $\|\mathcal{X}\|_{F,1} = \sum_{i_1, i_2} \|\mathcal{X}_{i_1, i_2, \dots, i_N}\|_F$ , respectively. Supposing that the vector  $\mathbf{n}$  is a reordering of the vector  $[1, 2, \dots, N]$ . The vector  $\mathbf{n}$ -based **generalized tensor transposition** of  $\mathcal{X}$  is denoted as  $\vec{\mathcal{X}}^{\mathbf{n}} \in \mathbb{R}^{I_{n_1} \times I_{n_2} \times \dots \times I_{n_N}}$ , which is generated by rearranging the modes of  $\mathcal{X}$  in the order specified by the vector  $\mathbf{n}$ . The corresponding operation and its inverse operation are denoted as  $\vec{\mathcal{X}}^{\mathbf{n}} = \text{permute}(\mathcal{X}, \mathbf{n})$  and  $\mathcal{X} = \text{ipermute}(\vec{\mathcal{X}}^{\mathbf{n}}, \mathbf{n})$ , respectively. The **generalized tensor unfolding** of  $\mathcal{X}$  is a matrix defined as  $\mathbf{X}_{[\mathbf{n}_{1:d}; \mathbf{n}_{d+1:N}]} = \text{reshape}(\vec{\mathcal{X}}^{\mathbf{n}}, \prod_{i=1}^d I_{n_i}, \prod_{i=d+1}^N I_{n_i})$ . The corresponding inverse operation is defined as  $\mathcal{X} = \Upsilon(\mathbf{X}_{[\mathbf{n}_{1:d}; \mathbf{n}_{d+1:N}]})$ .

2) **FCTN framework:** Below, we introduce some key algebraic foundations under the FCTN decomposition framework, which will be used extensively throughout this paper. Please refer to the literatures [20], [21], [51] for more details.

**Definition II.1. (FCTN decomposition [20])** *The FCTN decomposition aims to decompose an order- $N$  tensor  $\mathcal{X} \in \mathbb{R}^{I_1 \times I_2 \times \dots \times I_N}$  into a series of order- $N$  factor tensors  $\mathcal{G}_k \in \mathbb{R}^{R_{1,k} \times R_{2,k} \times \dots \times R_{k-1,k} \times I_k \times R_{k,k+1} \times \dots \times R_{k,N}}$ , ( $k = 1, 2, \dots, N$ ). The element-wise form of the FCTN decomposition can be expressed as*

$$\begin{aligned} \mathcal{X}(i_1, i_2, \dots, i_N) = & \\ & \sum_{r_{1,2}=1}^{R_{1,2}} \sum_{r_{1,3}=1}^{R_{1,3}} \dots \sum_{r_{1,N}=1}^{R_{1,N}} \sum_{r_{2,3}=1}^{R_{2,3}} \dots \sum_{r_{2,N}=1}^{R_{2,N}} \dots \sum_{r_{N-1,N}=1}^{R_{N-1,N}} \\ & \{\mathcal{G}_1(i_1, r_{1,2}, r_{1,3}, \dots, r_{1,N}) \mathcal{G}_2(r_{1,2}, i_2, r_{2,3}, \dots, r_{2,N}) \dots \\ & \mathcal{G}_k(r_{1,k}, r_{2,k}, \dots, r_{k-1,k}, i_k, r_{k,k+1}, \dots, r_{k,N}) \dots \\ & \mathcal{G}_N(r_{1,N}, r_{2,N}, \dots, r_{N-1,N}, i_N)\}. \end{aligned} \quad (1)$$

The factors  $\mathcal{G}_1, \mathcal{G}_2, \dots, \mathcal{G}_N$  are the core tensors of  $\mathcal{X}$  and can be abbreviated as  $\{\mathcal{G}\}_{1:N}$ , then  $\mathcal{X} = \text{FCTN}(\{\mathcal{G}\}_{1:N})$ . The vector  $(R_{1,2}, R_{1,3}, \dots, R_{1,N}, R_{2,3}, R_{2,4}, \dots, R_{2,N}, \dots, R_{N-1,N})$  is defined as the FCTN-rank of the original tensor  $\mathcal{X}$ .

**Lemma II.1. (Transpositional Invariance [20])** *Supposing that an order- $N$  tensor  $\mathcal{X} \in \mathbb{R}^{I_1 \times I_2 \times \dots \times I_N}$  has the following FCTN decomposition:  $\mathcal{X} = \text{FCTN}(\mathcal{G}_1, \mathcal{G}_2, \dots, \mathcal{G}_N)$ . Then its vector  $\mathbf{n}$ -based generalized tensor transposition  $\vec{\mathcal{X}}^{\mathbf{n}}$  can be expressed as  $\vec{\mathcal{X}}^{\mathbf{n}} = \text{FCTN}(\vec{\mathcal{G}}_{n_1}^{\mathbf{n}}, \vec{\mathcal{G}}_{n_2}^{\mathbf{n}}, \dots, \vec{\mathcal{G}}_{n_N}^{\mathbf{n}})$ , where  $\mathbf{n} = (n_1, n_2, \dots, n_N)$  is a reordering of the vector  $(1, 2, \dots, N)$ .*

3) **Uniformly Dithered Quantization:** Below, we introduce the uniformly dithered quantization procedure for high-order tensor. It mainly involves the following two steps:

(I) **Dithering step:** This step is applied to tensor's entries that we plan to quantize. For instance, let  $y_k$  ( $\forall k \in [m]$ ) be the  $k$ -th noisy observation from the underlying tensor  $\mathcal{L}^* \in \mathbb{R}^{I_1 \times \dots \times I_N}$  via  $y_k = \langle \mathcal{P}_k, \mathcal{L}^* \rangle + \epsilon_k$ , where  $\mathcal{P}_k$  is the sampler that uniformly and randomly extracts one entry of  $\mathcal{L}^*$ , and  $\epsilon_k$  denotes additive noise. Then, we can obtain its dithered counterpart via  $y_k + \xi_k$ , where  $\xi_k$  refers to the dither generated from a uniform distribution on  $[-\frac{\delta}{2}, \frac{\delta}{2}]$  with some  $\delta > 0$ .

(II) **Quantization step:** In this step, we apply quantizer  $Q_{\delta}(\cdot)$  to all dithers  $y_k + \xi_k$ . Then, we attain the resulting dithered quantized measurements, i.e.,  $q_k = Q_{\delta}(y_k + \xi_k)$ . As presented in existing literature [60], [64]–[66], the quantizer  $Q_{\delta}(\cdot)$  utilized in this paper is set to be uniform scalar quantizer  $Q_{\delta}(\cdot) := \delta(\lfloor \cdot / \delta \rfloor + \frac{1}{2})$  with resolution  $\delta > 0$ .

The following Theorem II.1 demonstrates that the uniformly dithered quantized measurements exhibit statistical equivalence to the original data.

**Theorem II.1.** [66] *For quantizer  $Q_{\delta}(\cdot) := \delta(\lfloor \cdot / \delta \rfloor + \frac{1}{2})$  with resolution  $\delta > 0$ , and dither  $\xi \sim \text{Unif}([-\frac{\delta}{2}, \frac{\delta}{2}])$ , we have*

$$\mathbb{E}[Q_{\delta}(x + \xi)] = \mathbb{E}\left[\delta\left(\lfloor \frac{x + \xi}{\delta} \rfloor + \frac{1}{2}\right)\right] = x, \quad (2)$$

for any  $x \in \mathbb{R}$ , where the expectation is taken over  $\xi$ .

## III. FAST RANDOMIZED COMPRESSION ALGORITHMS FOR LARGE-SCALE HIGH-ORDER TENSOR

In this section, we devise fast and efficient randomized compression algorithms for large-scale high-order tensor. These compression techniques serve as the computational acceleration core of our proposed recovery algorithm framework.

### A. Proposed Fixed-Rank Randomized Algorithm

In this subsection, based on full-mode random projection, UTV factorization, and subspace iteration techniques, we put forward an efficient randomized algorithm for representation and compression of large-scale high-order tensors.

**Algorithm Description:** At each stage of Algorithm 1, the core tensor  $\mathcal{C}$  is unfolded, and the factor matrix  $\mathbf{F}_{\rho_v}$  is formed by taking the first  $r_{\rho_v}$  left singular vectors. The new core tensor  $\mathcal{C}^{(v)}$  is obtained by projecting the previous core tensor onto the subspace spanned by the columns of  $\mathbf{F}_{\rho_v}$ . We then have a  $v$ -th partial approximation, defined as  $\hat{\mathcal{X}}^{(v)} = \mathcal{C}^{(v)} \times_{i=1}^v \mathbf{F}_{\rho_i}$ . For convenience, given a processing order  $\rho := [1, 2, 3, \dots, N]$ , we define

$$z_1 = I_2 \dots I_d, z_j = \left( \prod_{i=\rho_1}^{\rho_{j-1}} r_i \right) \left( \prod_{i=\rho_{j+1}}^{\rho_N} I_i \right), \quad j = 2, \dots, N.$$

---

**Algorithm 1:** Fixed-Rank Randomized Compression.

---

**Input:**  $\mathcal{X} \in \mathbb{R}^{I_1 \times \dots \times I_N}$ , target rank:  $\mathbf{r} = (r_1, \dots, r_N)$ , sketch size:  $\mathbf{l} = (l_1, \dots, l_N)$ , processing order:  $q$ , oversampling parameter:  $p$ , power iteration:  $q$ .

**Output:**  $\hat{\mathcal{X}} = [\mathcal{C}; \mathbf{F}_1, \mathbf{F}_2, \dots, \mathbf{F}_N]$ .

- 1 Set  $\mathcal{C}^{(0)} \leftarrow \mathcal{X}$ ;
- 2 **for**  $v = 1, 2, \dots, \text{length}(\rho)$  **do**
- 3     Set  $\mathbf{A} \leftarrow \mathbf{C}_{(\rho_v)}^{(v-1)}$ ,  $[m, n] = \text{size}(\mathbf{A})$ ;
- 4     Initialize  $\mathbf{l}_{\rho_v}$ :  $\mathbf{r}_{\rho_v} + p \leq \mathbf{l}_{\rho_v} \leq \min\{m, n\}$ , and draw a random sketching matrix  $\mathbf{G}^{(v)} \in \mathbb{R}^{z_v \times l_{\rho_v}}$ ;
- 5     Let  $\mathbf{T}_2 = \mathbf{G}^{(v)}$ ;
- 6     **for**  $j = 1 : q + 1$  **do**
- 7          $\mathbf{T}_1 = \mathbf{A} \cdot \mathbf{T}_2$ ,  $\mathbf{T}_2 = \mathbf{A}^T \cdot \mathbf{T}_1$ ;
- 8     **end**
- 9     Do QR factorizations:  $\mathbf{T}_1 = \mathbf{Q}_1 \mathbf{R}_1$ ,  $\mathbf{T}_2 = \mathbf{Q}_2 \mathbf{R}_2$ ;
- 10     Compute  $\mathbf{D} = \mathbf{Q}_1^T \mathbf{A} \mathbf{Q}_2$ , or  $\mathbf{D} = \mathbf{Q}_1^T \mathbf{T}_1 (\mathbf{Q}_2^T \mathbf{T}_2)^\dagger$ ;
- 11     Compute a QRCP:  $\mathbf{D} = \tilde{\mathbf{Q}} \tilde{\mathbf{R}} \tilde{\mathbf{P}}^T$ ;
- 12     Form the UT $\mathbf{V}$ -based low-rank approximation:
- 13          $\mathbf{U}^{(v)} \leftarrow \mathbf{Q}_1 \cdot \tilde{\mathbf{Q}}$ ,  $\mathbf{T}^{(v)} \leftarrow \tilde{\mathbf{R}}$ ,  $\mathbf{V}^{(v)} \leftarrow \mathbf{Q}_2 \cdot \tilde{\mathbf{P}}$ ;
- 14         Update  $\mathbf{F}_{\rho_v} \leftarrow \mathbf{U}^{(v)}(:, 1 : \mathbf{r}_{\rho_v})$ ,  $\mathbf{C}_{(\rho_v)}^{(v)} \leftarrow (\mathbf{F}_{\rho_v})^T \mathbf{C}_{(\rho_v)}^{(v-1)}$ ;
- 15          $\mathcal{C}^{(v)} \leftarrow \mathbf{C}_{(\rho_v)}^{(v)}$ , in tensor format.
- 16 **end**
- 17  $\hat{\mathcal{X}} = \mathcal{C} \times_1 \mathbf{F}_1 \times_2 \mathbf{F}_2 \dots \times_N \mathbf{F}_N$ ;

---

For tensors whose singular values of unfolded matrices exhibit a certain degree of decay, the proposed Algorithm 1 may be sufficiently accurate when  $q = 0$ . However, in applications where the unfolding matrices of the target tensor display a slowly decaying singular values, it may obtain the approximation result that deviate significantly from the exact ones (computed by the THOSVD [67] and STHOSVD [68]). Thus, we incorporate  $q$  steps of a power iteration to improve the accuracy of the proposed randomized compression algorithm in these circumstances.

Below, we mainly clarify the differences between our proposed algorithm and existing related methods [61], [69].

- When performing compressed representation for each mode of the target tensor, the proposed method leverages a sketch of the core tensor's unfolding matrix in order to project it onto its row space, i.e., *Line 7 in Algorithm 1*. This i) significantly improves the quality of the approximate basis  $\mathbf{Q}_2$  and, as a result, the quality of the approximate right singular subspace of  $\mathbf{A}$  compared to that of two-sided sketching based STHOSVD method [69], which utilizes a random matrix for the projection, and ii) allows  $\mathbf{D}_{\text{approx}} = \mathbf{Q}_1^T \mathbf{T}_1 (\mathbf{Q}_2^T \mathbf{T}_2)^\dagger$  to provide a highly accurate approximation to  $\mathbf{D} = \mathbf{Q}_1^T \mathbf{A} \mathbf{Q}_2$ .
- The proposed method applies a column-pivoted QR decomposition to small-size compressed matrix  $\mathbf{D}$ , i.e., *Line 11 in Algorithm 1*. Whereas, the R-STHOSVD [61] utilizes a truncated SVD to decompose the compressed matrix. Compared to the latter, the former can boost the computational efficiency.

---

**Algorithm 2:** Fixed-Accuracy Randomized Compression.

---

**Input:**  $\mathcal{X} \in \mathbb{R}^{I_1 \times \dots \times I_N}$ , processing order:  $\rho$ , error tolerance:  $\epsilon$ , block size:  $b$ , power parameter:  $q$ .

**Output:**  $\hat{\mathcal{X}} = [\mathcal{C}; \mathbf{F}_1, \mathbf{F}_2, \dots, \mathbf{F}_d]$ .

- 1 Set  $\mathcal{C}^{(0)} \leftarrow \mathcal{X}$ ;
- 2 **for**  $v = 1, 2, \dots, \text{length}(\rho)$  **do**
- 3     Set  $\mathbf{A} \leftarrow \mathbf{C}_{(\rho_v)}^{(v-1)}$ ,  $n = \text{size}(\mathbf{A}, 2)$ ;
- 4      $\mathbf{Y}^{\{v\}} = [\dots]$ ;  $\mathbf{W}^{\{v\}} = [\dots]$ ;
- 5      $E = \|\mathbf{A}\|_F^2$ ,  $\text{tol} \leftarrow \epsilon^2$ ;
- 6     **for**  $i = 1, 2, 3, \dots$  **do**
- 7         Generate a random sketching matrix  $\Omega_i \in \mathbb{R}^{z_v \times b}$ ,  $\alpha \leftarrow 0$ ;
- 8         **for**  $j = 1, 2, \dots, q$  **do**
- 9              $\mathbf{W}^{(i)} \leftarrow \mathbf{A}^T \mathbf{A} \Omega_i - \mathbf{W}^{\{v\}} \mathbf{Z}^{-1} (\mathbf{W}^{\{v\}})^T \Omega_i - \alpha \Omega_i$ ;
- 10              $[\Omega_i, \hat{S}, \sim] = \text{eigSVD}(\mathbf{W}^{(i)})$ ;
- 11             **if**  $j > 1$  and  $\alpha < \hat{S}(b, b)$  **then**
- 12                  $\alpha \leftarrow (\hat{S}(b, b) + \alpha)/2$ ;
- 13         **end**
- 14          $\mathbf{Y}^{(i)} = \mathbf{A} \Omega_i$ ,  $\mathbf{W}^{(i)} = \mathbf{A}^T \mathbf{Y}^{(i)}$ ;
- 15          $\mathbf{Y}^{\{v\}} = [\mathbf{Y}^{(v)}, \mathbf{Y}^{(i)}]$ ,  $\mathbf{W}^{\{v\}} = [\mathbf{W}^{\{v\}}, \mathbf{W}^{(i)}]$ ;
- 16          $\mathbf{Z} = (\mathbf{Y}^{\{v\}})^T \mathbf{Y}^{\{v\}}$ ,  $\mathbf{T} = (\mathbf{W}^{\{v\}})^T \mathbf{W}^{\{v\}}$ ;
- 17         **if**  $E - \text{tr}(\mathbf{T} \mathbf{Z}^{-1}) < \epsilon^2$  **then**
- 18             **break**;
- 19         **end**
- 20     **end**
- 21      $[\hat{\mathbf{V}}, \hat{\mathbf{D}}] = \text{eig}(\mathbf{Z})$ ;
- 22      $\mathbf{U}^{\{v\}} = \mathbf{Y}^{\{v\}} \hat{\mathbf{V}} \left( \sqrt{\hat{\mathbf{D}}} \right)^{-1}$ ;
- 23     Update  $\mathbf{F}_{\rho_v} \leftarrow \mathbf{U}^{\{v\}}$ ,  $\mathbf{C}_{(\rho_v)}^{(v)} \leftarrow (\mathbf{F}_{\rho_v})^T \mathbf{C}_{(\rho_v)}^{(v-1)}$ ;
- 24      $\mathcal{C}^{(v)} \leftarrow \mathbf{C}_{(\rho_v)}^{(v)}$ , in tensor format.
- 25 **end**

---

### B. Proposed Fixed-Precision Randomized Algorithm

The previous algorithm assume prior knowledge of the multi-linear rank. However, in practice, estimating the multi-linear rank of the target tensor can be challenging. Thus, we introduce an adaptive randomized algorithm for large-scale tensor compression, where the multi-linear rank is unknown.

**Algorithm Description:** For a given large-scale tensor  $\mathcal{X}$ , it is often desirable to effectively and accurately find a approximate decomposition  $\hat{\mathcal{X}}$  such that  $\|\mathcal{X} - \hat{\mathcal{X}}\|_F \leq \epsilon \|\mathcal{X}\|_F$ , where  $0 < \epsilon < 1$  is a user-defined parameter. To solve the aforementioned problem of fixed-precision approximation, several adaptive randomized algorithms for large-scale tensors have been proposed in the literature [61], [62]. The core idea of these existing methods is to first develop effective and adaptive randomized algorithm in the matrix format, and then apply it either separately or sequentially to the mode-unfolding matrices of large tensor. Finally, they will return a compressed small-scale core tensor and factor matrices.

Our proposed fixed-accuracy randomized method is presented in Algorithm 2, which is developed by the novel incremental QB approximation for enhanced parallel efficiency and the shifted power iteration for better accuracy.

- **Incremental QB approximation imposed on mode- $v$  unfolding  $\mathbf{C}_{(v)}^{(v-1)}$ :** For each  $v$ ,  $v \in \{1, 2, \dots, N\}$ ,

assume that  $\Omega \in \mathbb{R}^{z_v \times k}$  is a random sketching matrix, let  $\mathbf{A} := \mathbf{C}_{(v)}^{(v-1)} \in \mathbb{R}^{I_v \times z_v}$ ,  $\mathbf{Y} = \mathbf{A}\Omega$ ,  $\mathbf{W} = \mathbf{A}^T\mathbf{Y}$ , and the economic SVD of  $\mathbf{Y}$  be  $\mathbf{Y} = \hat{\mathbf{U}}\hat{\Sigma}\hat{\mathbf{V}}^T$ . Then, setting

$$\mathbf{Q} = \mathbf{Y}\hat{\mathbf{V}}\hat{\Sigma}^{-1}, \mathbf{B} = (\mathbf{W}\hat{\mathbf{V}}\hat{\Sigma}^{-1})^T. \quad (3)$$

And, if  $\text{tr}(\cdot)$  denotes the trace of a matrix,

$$\|\mathbf{A} - \mathbf{Q}\mathbf{B}\|_F^2 = \|\mathbf{A}\|_F^2 - \text{tr}(\mathbf{W}^T\mathbf{W}(\mathbf{Y}^T\mathbf{Y})^{-1}). \quad (4)$$

The novel QB approximation mentioned above enables us to calculate  $\mathbf{Y} = \mathbf{A}\Omega$ ,  $\mathbf{W} = \mathbf{A}^T\mathbf{Y}$  incrementally to generate the matrices  $\mathbf{Q}$  and  $\mathbf{B}$  at the end of process. This strategy differs from the previous *randQB-EI* approach proposed in [70], which computes  $\mathbf{Q}$  and  $\mathbf{B}$  incrementally with multiple QR decompositions. Besides, a new approach can be derived for evaluating the approximation error in the Frobenius norm according to (4).

- **Shifted power iteration scheme:** Under the above QB approximation framework, a more effective power iteration strategy can be developed. Specifically,  $\mathbf{W}_i = \mathbf{H}^T\mathbf{H}\Omega_i$  is computed in each step of the power iteration, where  $\Omega_i$  denotes small-block random matrix,  $\mathbf{H} = \mathbf{A} - \mathbf{Q}\mathbf{B}$ . In virtue of Equation (4) and the formulation of  $\mathbf{W} = \mathbf{A}^T\mathbf{Y}$ ,  $\mathbf{Y} = \mathbf{A}\Omega$ ,  $\mathbf{Z} = \mathbf{Y}^T\mathbf{Y}$ ,  $\mathbf{A} - \mathbf{Q}\mathbf{B}$  can be denoted by  $\mathbf{A} - \mathbf{Y}\mathbf{Z}^{-1}\mathbf{W}^T$ . Thus, combining  $\mathbf{T}_i \leftarrow \mathbf{A}\Omega_i - \mathbf{Y}\mathbf{Z}^{-1}\mathbf{W}^T\Omega_i$ ,  $\mathbf{W}_i \leftarrow \mathbf{A}^T\mathbf{T}_i - \mathbf{W}\mathbf{Z}^{-1}\mathbf{Y}^T\mathbf{T}_i$ , and  $\mathbf{W} = \mathbf{A}^T\mathbf{Y}$ , we can derive that

$$\mathbf{W}_i \leftarrow \mathbf{A}^T\mathbf{A}\Omega_i - \mathbf{W}\mathbf{Z}^{-1}(\mathbf{W})^T\Omega_i.$$

To further improve the approximation accuracy, the shift module is dynamically introduced, thus leading to the shifted power iteration scheme [71], [72], i.e.,

$$\mathbf{W}_i \leftarrow \mathbf{A}^T\mathbf{A}\Omega_i - \mathbf{W}\mathbf{Z}^{-1}(\mathbf{W})^T\Omega_i - \alpha\Omega_i.$$

The two modules involved in the proposed algorithm essentially replace the QR decomposition in the *randQB-EI* method [70] with some matrix skills to enhance parallel efficiency. When the power parameter is set to be  $q = 0, 1, 2$ , the proposed algorithm is actually equivalent to the adaptive R-STHOSVD algorithms [61], [62] using *randQB-EI* technique. For  $q > 2$ , the shifted parameter  $\alpha$  is dynamically updated to enhanced accuracy.

### C. Theoretical Analysis on Error Upper Bounds

For the sake of conciseness in the proof, the processing order is set to be  $\rho := [1, 2, \dots, N]$ . Without loss of generality, let  $I'_v = \min\{I_v, r_v \dots r_{v-1}I_{v+1} \dots I_N\}$ ,  $v = 1, 2, \dots, N$ . In order to facilitate the representation of the two dimensions of intermediate matrix  $\mathbf{C}_{(v)}^{(v-1)}$ , we define

$$z_1 = I_2 I_3 \dots I_d, \quad z_j = \left( \prod_{i=1}^{j-1} r_i \right) \left( \prod_{i=j+1}^N I_i \right), \quad j = 2, \dots, N.$$

For each  $v$ , the *Singular Value Decomposition* (SVD) of

$\mathbf{C}_{(v)}^{(v-1)} = \mathbf{U}^{(v)}\Sigma^{(v)}(\mathbf{V}^{(v)})^T$  is further denoted as follows:

$$\mathbf{C}_{(v)}^{(v-1)} = \left[ \mathbf{U}_1^{(v)} \mathbf{U}_2^{(v)} \right] \begin{bmatrix} \Sigma_1^{(v)} & \\ & \Sigma_2^{(v)} \end{bmatrix} \begin{bmatrix} \mathbf{V}_1^{(v)} \\ \mathbf{V}_2^{(v)} \end{bmatrix}^T, \quad (5)$$

$$\begin{aligned} \mathbf{U}_1^{(v)} &= \mathbf{U}^{(v)}(:, 1 : l_v - p), \quad \mathbf{U}_2^{(v)} = \mathbf{U}^{(v)}(:, l_v - p + 1 : I'_v), \\ \mathbf{V}_1^{(v)} &= \mathbf{V}^{(v)}(:, 1 : l_v - p), \quad \mathbf{V}_2^{(v)} = \mathbf{V}^{(v)}(:, l_v - p + 1 : I'_v), \\ \Sigma_1^{(v)} &= \Sigma^{(v)}(1 : r_v, 1 : r_v), \text{ and } \Sigma_2^{(v)} = \Sigma^{(v)}(r_v + 1 : I'_v, r_v + 1 : I'_v). \end{aligned}$$

Furthermore, we define  $\Psi_1^{(v)} \in \mathbb{R}^{(l_v - p) \times l_v}$  and  $\Psi_2^{(v)} \in \mathbb{R}^{(I'_v - l_v + p) \times l_v}$  as follows:

$$\Psi_1^{(v)} = (\mathbf{V}_1^{(v)})^T \cdot \mathbf{G}^{(v)}, \quad \Psi_2^{(v)} = (\mathbf{V}_2^{(v)})^T \cdot \mathbf{G}^{(v)}. \quad (6)$$

We assume that  $\Psi_1^{(v)}$  is full row rank and its pseudo-inverse satisfies  $\Psi_1^{(v)} \cdot (\Psi_1^{(v)})^\dagger = \mathbf{I}$ ,  $v = 1, 2, \dots, N$ .

Based on the aforementioned preliminaries, we now primarily focus on providing an error upper bound analysis for Algorithm 1. Please see Theorem III.1 for more details.

**Theorem III.1.** *Let  $\hat{\mathbf{X}} = \mathcal{C} \times_1 \mathbf{F}_1 \times_2 \mathbf{F}_2 \dots \times_N \mathbf{F}_N$  be the low multilinear rank- $(r_1, r_2, \dots, r_N)$  approximation of an order- $N$  tensor  $\mathbf{X} \in \mathbb{R}^{I_1 \times I_2 \times \dots \times I_N}$  by Algorithm 1 with processing order  $\rho := [1, 2, \dots, N]$ , sketch size:  $\mathbf{l} = (l_1, l_2, \dots, l_N)$ , and oversampling parameter  $p \geq 2$  satisfying*

$$r_j + p \leq l_j \leq \min\{I_j, z_j\}, \quad j = 1, 2, \dots, N.$$

For each  $v$ , assume that  $\Psi_1^{(v)}$  is of full row rank. Let  $\hat{\mathbf{X}}_{\text{opt}}$  denote the optimal rank- $\mathbf{r}$  approximation,  $\tau_1 = \sigma_{r_v}(\mathbf{C}_{(v)}^{(v-1)})$ ,  $\tau_2 = \sigma_{l_v - p + 1}(\mathbf{C}_{(v)}^{(v-1)})$ ,  $\tau_3 = \sigma_1(\mathbf{C}_{(v)}^{(v-1)})$ . Then, we have

$$\begin{aligned} \|\mathbf{X} - \hat{\mathbf{X}}\|_F^2 &\leq \sum_{v=1}^N \left\{ \left( \sqrt{\frac{(\alpha^{(v)})^2 \omega^2}{1 + (\beta^{(v)})^2 \omega^2}} + \sqrt{\frac{(\eta^{(v)})^2 \omega^2}{1 + (\xi^{(v)})^2 \omega^2}} \right. \right. \\ &\quad \left. \left. + \|\mathbf{X} - \hat{\mathbf{X}}_{\text{opt}}\|_F \right)^2 + \frac{(\alpha^{(v)})^2 \omega^2}{1 + (\beta^{(v)})^2 \omega^2} \right\}, \end{aligned} \quad (7)$$

where  $\alpha^{(v)} = \sqrt{r_v \frac{\tau_2^2}{\tau_1} (\frac{\tau_2}{\tau_1})^{2q}}$  ( $q$  denotes the power iteration parameter),  $\beta^{(v)} = \frac{\tau_2^2}{\tau_1 \tau_3} (\frac{\tau_2}{\tau_1})^{2q}$ ,  $\eta^{(v)} = \frac{\tau_1}{\tau_2} \alpha^{(v)}$ ,  $\xi^{(v)} = \frac{1}{\tau_2} \beta^{(v)}$ , and  $\omega_1 = \|\Psi_2^{(v)}\|_2$ ,  $\omega_2 = \|(\Psi_1^{(v)})^\dagger\|_2$ ,  $\omega = \omega_1 \omega_2$ .

Next, we provide the explicit error-upper-bounds for the proposed Algorithm 1, which, in contrast to the argument in Theorem III.1, depends on distributional assumptions on the random matrix  $\{\mathbf{G}^{(v)}\}_{v=1}^N$ . Below, we mainly conduct theoretical analysis from different sketching matrices  $\{\mathbf{G}^{(v)}\}_{v=1}^N$ , such as the standard Gaussian matrices, the uniform random matrices, the Kronecker products of *Subsampled Randomized Fourier Transform* (SRFT) matrices, and the *Khatri-Rao* (KR) products of the standard Gaussian matrices (or the uniform random matrices).

**Theorem III.2. (Gaussian Sketching)** *For each  $v$ , we assume that  $\mathbf{G}^{(v)}$ ,  $v = 1, 2, \dots, N$  is a standard Gaussian sketching matrix. With the notation of Theorem III.1, we obtain the*

average error bound for Algorithm 1, i.e.,

$$\mathbb{E}_{\{\mathbf{G}^{(v)}\}_{v=1}^N} \|\mathbf{X} - \hat{\mathbf{X}}\|_F \leq \left( \sum_{v=1}^N \left( \left( \|\mathbf{X} - \hat{\mathbf{X}}_{\text{opt}}\|_F + \left\{ \left( 1 + \frac{\tau_2}{\tau_1} \right) \sqrt{r_v} \phi^{(v)} \tau_2 \left( \frac{\tau_2}{\tau_1} \right)^{2q} \right\} \right)^2 + \frac{(\alpha^{(v)})^2 (\phi^{(v)})^2}{1 + (\beta^{(v)})^2 (\phi^{(v)})^2} \right)^{\frac{1}{2}} \right), \quad (8)$$

where  $\phi^{(v)} = \frac{4e\sqrt{l_v}}{p+1} (\sqrt{\min\{I_j, z_j\}} - l_v + p + \sqrt{l_v} + 7)$ .

**Theorem III.3. (KR-Gaussian Sketching)** For each  $v$ ,  $v \in \{1, \dots, N\}$ , we assume that  $\mathbf{G}^{(v)}$  is the Khatri-Rao product of the standard Gaussian matrices. By setting  $\omega = \frac{\sqrt{l_v} + t \sqrt{\prod_{m=1}^{v-1} (\sqrt{T_m} + t) \prod_{m=v+1}^N (\sqrt{r_m} + t)}}{\sqrt{l_v} - t \sqrt{\prod_{m=1}^{v-1} (\sqrt{r_m} + t) \prod_{m=v+1}^N (\sqrt{I_m} + t)}}$  in (7), we obtain the error bound for Algorithm 1 with probability at least

$$1 - 2 \sum_{v=1}^N \left\{ (\mathbf{l}_v - p) \cdot \exp(-c_v t^2) + (I'_v - \mathbf{l}_v + p) \cdot \exp(-c'_v t^2) \right\} - 2 \sum_{v=1}^N \sum_{k=1}^{\mathbf{l}_v} \sum_{h \neq v} \exp(-c_{v,k,h} t^2 / K_{v,k,h}^2),$$

for every  $t \geq 0$ . Here, for each  $v, k, h$  ( $v \neq h$ ),  $c_v, c'_v$ , and  $c_{v,k,h}$  are absolute constants,  $K_{v,k,h}$  satisfies the following equation:

$$K_{v,k,h} = \begin{cases} \max_{i_v=1,2,\dots,r_v} \|\Omega_{v,h}(i_v, k)\|_{\psi_2}, & \text{if } h < v; \\ \max_{i_v=1,2,\dots,I_v} \|\Omega_{v,h}(i_v, k)\|_{\psi_2}, & \text{if } h > v. \end{cases}$$

**Theorem III.4. (Uniform Sketching)** For each  $v$ , we assume that  $\mathbf{G}^{(v)}, v = 1, 2, \dots, N$  is a uniform sketching matrix. By setting  $\omega = \omega_1 \omega_2$ ,  $\omega_1 = a_{v,1} \sqrt{\max\{I'_v - \mathbf{l}_v + p, \mathbf{l}_v\}}$ ,  $\omega_2 = c_{v,1} \sqrt{l_v}$ ,  $\mathbf{l}_v > (1 + 1/\ln(\mathbf{l}_v - p))(\mathbf{l}_v - p)$  in (7), we obtain the error upper bound for Algorithm 1 with probability at least

$$1 - \sum_{v=1}^N \left\{ \exp(-a_{v,2} \cdot \max\{I'_v - \mathbf{l}_v + p, \mathbf{l}_v\}) + \exp(-c_{v,2} \cdot \mathbf{l}_v) \right\}.$$

Here, for each  $v$ , we define  $a_{v,1}, a_{v,2}, c_{v,1}, c_{v,2}$  as positive constants with  $a_{v,1} = 6\alpha_v \sqrt{a_{v,2} + 4}$  and  $\alpha_v > 1$ .

**Theorem III.5. (KR-Uniform Sketching)** For each  $v$ ,  $v \in \{1, 2, \dots, N\}$ , we assume that  $\mathbf{G}^{(v)}$  is the Khatri-Rao product of the uniform random matrices. By setting  $\omega = \omega_1 \omega_2$ ,  $\omega_1 = \sqrt{l_v} + C_v \sqrt{I'_v - \mathbf{l}_v + p + t}$ ,  $\omega_2 = \frac{1}{\sqrt{l_v} - C'_v \sqrt{l_v - p} - t}$  in (7), we obtain the error bound for Algorithm 1 with probability at least

$$1 - 2 \sum_{v=1}^N \left\{ \exp(-c_v t^2) + \exp(-c'_v t^2) \right\},$$

for every  $t \geq 0$ . Here, for each  $v$ ,  $C_v = C_{K_v}$  and  $c_v = c_{K_v} \geq 0$  depend only on the sub-Gaussian norm

$$K_v = \max_{j=1,2,\dots,l_v} \|(\Psi_2^{(v)})^T(j, :) \|_{\psi_2} = \max_{j=1,2,\dots,l_v} \|\Psi_2^{(v)}(:, j)\|_{\psi_2},$$

and  $C'_v = C_{K'_v}$  and  $c'_v = c_{K'_v} \geq 0$  depend only on the sub-Gaussian norm

$$K'_v = \max_{j=1,2,\dots,l_v} \|(\Psi_1^{(v)})^T(j, :) \|_{\psi_2} = \max_{j=1,2,\dots,l_v} \|\Psi_1^{(v)}(:, j)\|_{\psi_2}.$$

**Theorem III.6. (Kronecker-SRFT Sketching)** For each  $v$ ,  $v \in$

$\{1, 2, \dots, N\}$ , we assume that  $\mathbf{G}^{(v)}$  is the Kronecker products of SRFT matrices. By setting  $\omega = \sqrt{\kappa_1^{(v)} z_v / l_v}$  in (7), we obtain the error bound for Algorithm 1 with probability at least  $1 - 2 \sum_{v=1}^N 1/\kappa_2^{(v)}$ . Here, the sequences  $\kappa_1^{(v)} > 1$  and  $\kappa_2^{(v)} > 1$  ( $v \in \{1, 2, \dots, N\}$ ) satisfy

$$\min_{v,h} \{S_{v,h}\} \geq \frac{(\kappa_1^{(v)})^2 \kappa_2^{(v)}}{(\kappa_1^{(v)} - 1)^2} [(\mathbf{l}_v - p)^2 + (\mathbf{l}_v - p)],$$

where  $z_v = r_1 r_2 \dots r_{v-1} I_{v+1} \dots I_N$ ,  $\mathbf{l}_v = \prod_{h=1}^N S_{v,h}$ .

#### IV. GENERALIZED NONCONVEX APPROACH FOR MULTI-DIMENSIONAL DATA MODELING

In this section, under the framework of FCTN decomposition, we develop a novel generalized nonconvex gradient-domain regularization approach tailored for high-order tensors. This regularization strategy lays the foundation for the model establishment of subsequent multi-dimensional data recovery.

##### A. Generalized Nonconvex Regularizers

1) *Novel regularizer encoding prior structures*: In many application scenarios, the large-scale multi-dimensional data to be estimated are not only with low-rankness but also possess significant smooth structure. As exemplified in the supplementary materials, the color images/videos, hyperspectral images/videos, MRI datasets and face datasets represented by high-order tensors fromat exhibit strong global low-rankness (**L**) due to the strong sparsity of singular values obtained through generalized tensor unfolding, as well as strong local smoothness (**S**) resulting from the strong sparsity of their gradient tensors. Therefore, a natural idea is how to simultaneously promote these two types of equivalent sparsity through a concise yet effective regularization method, so as to deeply mine insightful **L+S** prior features latent in multi-dimensional data. In response to the aforementioned, we consider investigating novel generalized nonconvex gradient-domain regularizer within the FCTN decomposition, which can simultaneously encode essential **L+S** prior features underlying high-order tensors.

We begin by stating a few definitions and lemmas that are utilized later on.

**Definition IV.1. (Gradient tensor)** For  $\mathcal{A} \in \mathbb{R}^{I_1 \times \dots \times I_N}$ , its gradient tensor along the  $t$ -th mode is defined as

$$\mathcal{G}_t := \nabla_t(\mathcal{A}) = \mathcal{A} \times_t \mathbf{D}_{I_t}, \quad t = 1, 2, \dots, N, \quad (9)$$

where  $\mathbf{D}_{I_t}$  is a row circulant matrix of  $(-1, 1, 0, \dots, 0)$ ,  $\nabla_t$  is defined as the corresponding difference operator along the  $t$ -th mode of tensor  $\mathcal{A}$ , and  $\mathcal{A} \times_t \mathbf{D}_{I_t}$  denotes the mode- $t$  product of tensor  $\mathcal{A}$  with matrix  $\mathbf{D}_{I_t}$ .

**Definition IV.2.** [20] Supposing that  $\mathbf{X} \in \mathbb{R}^{I_1 \times I_2 \times \dots \times I_N}$  is an order- $N$  tensor and the vector  $\mathbf{n}$  is a specified rearrangement of the vector  $[1, 2, \dots, N]$ . Then, the generalized tensor unfolding of  $\mathbf{X}$  is defined as a matrix  $\mathbf{X}_{[\mathbf{n}_{1:d}; \mathbf{n}_{d+1:N}]} = \text{reshape}(\tilde{\mathbf{X}}^{\mathbf{n}}, \prod_{i=1}^d I_{\mathbf{n}_i}, \prod_{i=d+1}^N I_{\mathbf{n}_i})$ . The corresponding inverse operation is defined as  $\mathbf{X} = \Upsilon(\mathbf{X}_{[\mathbf{n}_{1:d}; \mathbf{n}_{d+1:N}]})$ .

The following Lemma indicates that the FCTN-rank can bound the rank of all generalized tensor unfolding.

**Lemma IV.1.** [20] *Supposing that an order- $N$  tensor  $\mathcal{X} \in \mathbb{R}^{I_1 \times I_2 \times \cdots \times I_N}$  can be represented by equation (1), then the following inequality holds:*

$$\text{Rank}(\mathcal{X}_{[\mathbf{n}_{1:d}; \mathbf{n}_{d+1:N}]}) \leq \prod_{i=1}^d \prod_{j=d+1}^N R_{\mathbf{n}_i, \mathbf{n}_j}, \quad (10)$$

where  $R_{\mathbf{n}_i, \mathbf{n}_j} = R_{\mathbf{n}_j, \mathbf{n}_i}$  if  $\mathbf{n}_i > \mathbf{n}_j$ , and  $(\mathbf{n}_1, \mathbf{n}_2, \dots, \mathbf{n}_N)$  is a reordering of the vector  $(1, 2, \dots, N)$ .

Below, we formally introduce the proposed gradient-domain regularizer named *FCTN-based Generalized Nonconvex Tensor Correlated Total Variation* (FCTN-GNTCTV).

For any  $\mathcal{X} \in \mathbb{R}^{I_1 \times I_2 \times \cdots \times I_N}$ , let  $\Gamma$  represent a priori set consisting of directions along which  $\mathcal{X}$  equips **L+S** priors, and  $\mathbf{G}_t, t \in \Gamma$  denote the gradient tensor along the  $t$ -th mode of  $\mathcal{X}$ . Then, the FCTN-GNTCTV regularizer is defined as follows:

$$\begin{aligned} \|\mathcal{X}\|_{\mathfrak{F}\mathfrak{N}} &:= \frac{1}{\gamma} \sum_{t \in \Gamma} \left\{ \sum_{k=1}^{\bar{N}} \alpha_k \cdot \|\mathbf{G}_{t[\mathbf{n}_1^k; \mathbf{n}_2^k]}\|_{\Phi} \right\}, \\ &= \frac{1}{\gamma} \sum_{t \in \Gamma} \left\{ \sum_{k=1}^{\bar{N}} \alpha_k \cdot \sum_i \Phi\left(\sigma_i(\mathbf{G}_{t[\mathbf{n}_1^k; \mathbf{n}_2^k]})\right) \right\}, \end{aligned} \quad (11)$$

where  $\{\alpha_k\}_{k=1}^{\bar{N}}$  are the non-negative weights with  $\sum_k \alpha_k = 1$ ,  $\gamma := \#\{\Gamma\}$  equals to the cardinality of  $\Gamma$ , where  $\mathbf{n}^k$  is the  $k$ -th permutation of the vector  $[1, 2, \dots, N]$ ,  $\mathbf{n}_1^k = \mathbf{n}_{1:N/2}^k$ ,  $\mathbf{n}_2^k = \mathbf{n}_{[N/2]+1:N}^k$ ,

$$\bar{N} = \begin{cases} C_N^{\lfloor N/2 \rfloor}, & \text{if } N \text{ is odd,} \\ C_N^{\lfloor N/2 \rfloor}/2, & \text{if } N \text{ is even,} \end{cases}$$

and  $\lfloor \cdot \rfloor$  denotes the floor function. The generalized nonconvex function  $\Phi(\cdot) : \mathbb{R} \rightarrow \mathbb{R}$  satisfies the following assumptions:

(I):  $\Phi(\cdot) : \mathbb{R} \rightarrow \mathbb{R}$  is proper, lower semi-continuous and symmetric with respect to y-axis;

(II):  $\Phi(\cdot)$  is concave and monotonically increasing on  $[0, \infty)$  with  $\Phi(0) = 0$ .

**Remark IV.1.** *Many popular nonconvex penalty functions  $\Phi(\cdot)$  satisfy the above assumptions, such as firm function [73], logarithmic (Log) function [74],  $\ell_q$  function [75], capped- $\ell_q$  function [76], [77], smoothly clipped absolute deviation (SCAD) function [78], and minimax concave penalty (MCP) function [79]. Thus, in the above gradient-domain regularizer (11), we effectively employ a family of nonconvex functions on the singular values of all generalized unfolding matrices derived from each gradient tensor.*

Below, we provide a mathematical explanation to elucidate how the proposed regularization method can simultaneously encode global low-rankness and local smoothness priors.

**Remark IV.2.** *For  $\mathcal{X} \in \mathbb{R}^{I_1 \times I_2 \times \cdots \times I_N}$  with FCTN-rank  $(R_{1,2}, R_{1,3}, \dots, R_{1,N}, R_{2,3}, R_{2,4}, \dots, R_{2,N}, \dots, R_{N-1,N})$ , it can be verified that*

$$R - 1 \leq \text{Rank}(\mathbf{G}_{t[\mathbf{n}_1^k; \mathbf{n}_2^k]}) \leq R, \quad (12)$$

where  $R = \prod_{i=1}^{\lfloor N/2 \rfloor} \prod_{j=\lfloor N/2 \rfloor+1}^N R_{\mathbf{n}_i^k, \mathbf{n}_j^k}$ . This reveals that the low-rankness between the original and resulting gradient tensors are consistent, demonstrating that the FCTN-GNTCTV regularizer can indirectly induce the expected **L**-prior feature of the original tensor like a low-rank regularizer.

From the perspective of **S**-prior encoding, we can also verify that

$$\|\mathcal{X}\|_{\text{TV}, \Phi} \lesssim \|\mathcal{X}\|_{\mathfrak{F}\mathfrak{N}} \lesssim \sqrt{R} \|\mathcal{X}\|_{\text{TV}, \Phi}. \quad (13)$$

Here,  $\|\cdot\|_{\text{TV}, \Phi}$  can be interpreted as a nonconvex extension of the TV-norm, which is defined as

$$\|\mathcal{X}\|_{\text{TV}, \Phi} := \sum_{t \in \Gamma} \|\nabla_t(\mathcal{A})\|_{\ell_1, \Phi} = \sum_{t \in \Gamma} \|\Phi \odot \nabla_t(\mathcal{A})\|_1,$$

where  $\odot$  denotes element-wise operation. Besides,  $\lesssim$  means that  $a \lesssim b \Leftrightarrow a \leq Cb$ ,  $C$  is a fixed absolute constant. The inequality (13) means that FCTN-GNTCTV and nonconvex TV are compatible in sense of norm, indicating that the proposed regularizer can also indirectly extract the expected **S**-prior of the targeted tensors like a TV regularizer.

2) **Novel noise/outliers regularizer:** To enhance the robustness against noise/outliers existed in high-order format, we define the following nonconvex regularization penalty, i.e.,

$$\Upsilon(\mathcal{E}) := \psi(h(\mathcal{E})), \quad (14)$$

where  $\psi(\cdot) : \mathbb{R} \rightarrow \mathbb{R}$  is a generalized nonconvex function, which has the same properties as  $\Phi(\cdot)$  in (11). Here, two types of corrupted noise/outliers are taken into account. When the noise/outlier tensor  $\mathcal{E}$  has tube-wise structure, and  $h(\cdot) = \|\cdot\|_{F,1}$  is defined as an  $\ell_{F,1}$ -norm. Then, we have

$$\Upsilon(\mathcal{E}) := \psi(\|\mathcal{E}\|_{F,1}) = \sum_{i_1=1}^{I_1} \sum_{i_2=1}^{I_2} \dots \psi\left(\|\mathcal{E}_{i_1 i_2 \dots}\|_F\right). \quad (15)$$

When the tensor  $\mathcal{E}$  is an entry-wise noise/outlier tensor,  $h(\cdot) = \|\cdot\|_1$  is defined as an  $\ell_1$ -norm. Then, we have

$$\Upsilon(\mathcal{E}) := \psi(\|\mathcal{E}\|_1) = \sum_{i_1=1}^{I_1} \sum_{i_2=1}^{I_2} \dots \sum_{i_N=1}^{I_N} \psi(|\mathcal{E}_{i_1 i_2 \dots i_N}|). \quad (16)$$

Next, we mainly revisit the commonly-used nonconvex sparsity-inducing penalties and the corresponding proximal mappings, which play a central role in developing subsequent tensor recovery algorithms. For a nonconvex penalty function  $\psi(\cdot)$ , its proximity operator is defined as

$$\text{Prox}_{\psi, \mu}(v) = \arg \min_x \left\{ \mu \cdot \psi(x) + \frac{1}{2}(x - v)^2 \right\}, \quad (17)$$

where  $\mu > 0$  is a penalty parameter. In the supplementary materials, we have summarized the proximity operators for several popular nonconvex regularization penalties, including firm-thresholding,  $\ell_q$ -thresholding, MCP, Log, and SCAD penalties. On this basis, we can address the following two types of crucial minimization problems. That is,

$$\text{Prox}_{\psi, \lambda}(\mathcal{E}) = \arg \min_{\mathcal{E}} \lambda \cdot \Upsilon(\mathcal{E}) + \frac{1}{2} \|\mathcal{E} - \mathcal{A}\|_F^2,$$

$$\mathfrak{D}_{\Phi, \tau}(\mathbf{Y}) = \arg \min_{\mathbf{Y}} \tau \cdot \|\mathbf{X}\|_{\Phi} + \frac{1}{2} \|\mathbf{X} - \mathbf{Y}\|_F^2.$$

## V. RELATED APPLICATIONS

In this section, we primarily investigate the large-scale high-order tensor recovery, where the model formulation is shifted from unquantized observation to quantized observation. The gradient-domain regularization method in Section IV functions as a modeling capability enhancement module, whereas the randomized compression technique in Section III serves as a computational acceleration module for algorithm design.

### A. Nonquantized High-Order Tensor Recovery

1) *Proposed Generalized Nonconvex Model*: On the basis of Subsection IV-A, this subsection proposes a generalized nonconvex robust tensor completion model under the FCTN framework (abbreviated as *FCTN-GNRTC*), i.e.,

$$\begin{aligned} & \min_{\mathcal{L}, \mathcal{E}} \frac{1}{\gamma} \sum_{t \in \Gamma} \left\{ \sum_{k=1}^{\bar{N}} \alpha_k \cdot \left\| \mathbf{G}_{t[\mathbf{n}_1^k; \mathbf{n}_2^k]} \right\|_{\Phi} \right\} + \lambda \cdot \psi(h(\mathcal{E})), \\ & \text{s.t. } \mathcal{G}_t = \nabla_t(\mathcal{L}), \quad \mathbf{P}_{\Omega}(\mathcal{L} + \mathcal{E}) = \mathbf{P}_{\Omega}(\mathcal{M}), \end{aligned} \quad (18)$$

where  $\mathcal{L}$  represents the underlying tensor with both low-rank and smooth structures,  $\mathcal{E}$  denotes the noise/outlier tensor,  $\mathcal{M}$  signifies the observed tensor,  $\Phi(\cdot)$  and  $\psi(\cdot)$  are the generalized nonconvex functions, and  $\lambda$  is a trade-off parameter. The meanings of other symbols remain the same as those defined in Equations (11) and (14). Note that when the noise/outlier tensor  $\mathcal{E}$  is set to be zero, the proposed FCTN-GNRTC model (18) degenerates into the following *FCTN-based Generalized Nonconvex Tensor Completion* (FCTN-GNTC) model:

$$\begin{aligned} & \min_{\mathcal{L}, \mathcal{E}} \frac{1}{\gamma} \sum_{t \in \Gamma} \left\{ \sum_{k=1}^{\bar{N}} \alpha_k \cdot \left\| \mathbf{G}_{t[\mathbf{n}_1^k; \mathbf{n}_2^k]} \right\|_{\Phi} \right\}, \\ & \text{s.t. } \mathcal{G}_t = \nabla_t(\mathcal{L}), \quad \mathbf{P}_{\Omega}(\mathcal{L}) = \mathbf{P}_{\Omega}(\mathcal{M}). \end{aligned} \quad (19)$$

2) *ADMM-Based Optimization Algorithm*: Considering the limitation imposed by the paper's length, we have moved the entire derivation of the ADMM optimization algorithm, along with its associated time complexity analysis and convergence analysis, to the supplementary materials section.

### B. Quantized High-Order Tensor Recovery

1) *Generalized Nonconvex Quantized Model*: In this subsection, we address the problem of robust tensor completion from uniform scalar quantization using the proposed FCTN-GNTCTV regularization method. Let  $u_k$  ( $\forall k \in [m]$ ) be the  $k$ -th corrupted observations from the low-rank plus smooth tensor  $\mathcal{L}$  and the noise/outlier tensor  $\mathcal{S}$  via  $u_k = \langle \mathcal{P}_k, \mathcal{L} + \mathcal{E} \rangle + \epsilon_k$ , where  $\mathcal{P}_k$  is a sampler that uniformly and randomly selects one entry from corrupted tensor  $\mathcal{L} + \mathcal{E}$ ,  $\epsilon_k$  refers to the additive Gaussian noise. Motivated by the fact that the uniformly quantized dithered observations are equal to their original counterparts in terms of expectation, we propose the following quantized observation model:

$$y_k = Q_{\delta}(u_k + \xi_k),$$

in which  $Q_{\delta}(\cdot) := \delta(\lfloor \cdot / \delta \rfloor + \frac{1}{2})$  represents a uniform scalar quantizer with resolution parameter  $\delta > 0$ , and dithers  $\xi_k$  are generated from a uniform distribution  $U([-\frac{\delta}{2}, \frac{\delta}{2}])$ .

Furthermore, to handle the incomplete tensor damaged by both Gaussian noise and sparse noise simultaneously, we propose the following generalized nonconvex robust tensor completion model in the quantized scenario. Specifically,

$$\begin{aligned} & \min_{\|\mathcal{L}\|_{\infty} \leq \alpha} \frac{1}{2m} \sum_{k=1}^m \left( \langle \mathcal{P}_k, \mathcal{L} + \mathcal{E} \rangle - y_k \right)^2 + \lambda_2 \cdot \psi(h(\mathcal{E})) \\ & + \frac{\lambda_1}{\gamma} \sum_{t \in \Gamma} \left\{ \sum_{k=1}^{\bar{N}} \alpha_k \cdot \left\| \mathbf{G}_{t[\mathbf{n}_1^k; \mathbf{n}_2^k]} \right\|_{\Phi} \right\}, \\ & \text{s.t. } \mathcal{G}_t = \nabla_t(\mathcal{L}), t \in \Gamma, \end{aligned} \quad (20)$$

where  $\lambda_1$  and  $\lambda_2$  are the regularization parameter,  $y_k$  denotes the quantized measurements. The meanings of other symbols remain the same as those defined in Equations (11) and (14). Note that when we disregard the sparse noise scenario (i.e.,  $\mathcal{E}$  is set to be zero), the proposed model (20) reduces to the following model:

$$\begin{aligned} & \min_{\|\mathcal{L}\|_{\infty} \leq \alpha} \frac{1}{2m} \sum_{k=1}^m \left( \langle \mathcal{P}_k, \mathcal{L} \rangle - Q_{\delta}(\langle \mathcal{P}_k, \mathcal{L} \rangle + \epsilon_k + \xi_k) \right)^2 \\ & + \frac{\lambda_1}{\gamma} \sum_{t \in \Gamma} \left\{ \sum_{k=1}^{\bar{N}} \alpha_k \cdot \left\| \mathbf{G}_{t[\mathbf{n}_1^k; \mathbf{n}_2^k]} \right\|_{\Phi} \right\}, \\ & \text{s.t. } \mathcal{G}_t = \nabla_t(\mathcal{L}), t \in \Gamma, \end{aligned} \quad (21)$$

where the symbols  $Q_{\delta}(\cdot)$ ,  $\mathcal{P}_k$ ,  $\epsilon_k$ ,  $\xi_k$ , and  $\lambda_1$  are the same as those defined in model (20). For brevity, the quantized tensor models (20) and (21) are abbreviated as *FCTN-GNQRTC* and *FCTN-GNQTC*, respectively. It is noteworthy that when the quantizer  $Q_{\delta}(\cdot) = \text{sign}(\cdot)$  is set to be sign function, the aforementioned methods are simplified to the versions corresponding to one-bit quantization scenario.

2) *ADMM-Based Optimization Algorithm*: In this subsection, the ADMM framework [80] is adopted to solve the proposed quantized models (20) and (21). Due to space constraints of this paper, we have placed the detailed ADMM optimization algorithms for solving Model (20) and Model (21), along with their corresponding time complexity analysis and convergence analysis in the supplementary materials.

## VI. EXPERIMENTAL RESULTS

In this section, we perform extensive experiments on synthetic and real-world tensor data to substantiate the superiority and effectiveness of the proposed tensor recovery approach. All the experiments are run on the following platforms: 1) Windows 11 and Matlab (R2020a) with an Intel(R) Core(TM) i9-14900KF CPU and 64GB memory; 2) Windows 10 and Matlab (R2022b) with an Intel(R) Xeon(R) Gold-6230 2.10GHz CPU and 128GB memory.

### A. Experimental Settings

1) *Experimental Datasets*: In our experiments, *Color Images* (CIs), *Color Videos* (CVs), *Multi-Temporal Remote Sensing Images* (MRSIs), *Hyperspectral Videos* (HVs), *Face Datasets*, and *Cardiac Magnetic Resonance Images* (MRIs) are utilized as the tested tensor datasets. Due to the limitation

of paper length, we present the detailed description of the experimental datasets in the supplementary materials.

**Type 1: Color Images (CIs):** This dataset includes four large-scale high-dimensional CIs, which are called as Maastricht-Bassin ( $2177 \times 3113 \times 3$ ), Wildpark ( $2749 \times 4116 \times 3$ ), WestLotto ( $2612 \times 4650 \times 3$ ), and Sunrise ( $3040 \times 4056 \times 3$ ), respectively. We download these large-scale CIs from the Google art project website<sup>1</sup>.

**Type 2: Color Videos (CVs):** This dataset includes four four-order CVs called Rush-hour, Johnny, Stockholm, Intotree, respectively. We download these large-scale CVs from the derf website<sup>2</sup>. Only the first 50 frames of each video sequence are selected as the tested CVs owing to the computational limitation, in which each frame has the size  $720 \times 1280 \times 3$ .

**Type 3: Multi-Temporal Remote Sensing Images (MRSIs):** This dataset mainly involves four fourth-order MRSIs, which are named SPOT-5<sup>3</sup> ( $2000 \times 2000 \times 4 \times 13$ ), Landsat-7 ( $4500 \times 4500 \times 6 \times 11$ ), T29RMM ( $5001 \times 5001 \times 4 \times 6$ ), and T22LGN<sup>4</sup> ( $5001 \times 5001 \times 4 \times 7$ ), respectively. To speed up the calculation process, the spatial size of these MRSIs is downsampled (resized) to  $1000 \times 1000$ .

**Type 4: Hyperspectral Videos (HVs):** This dataset includes three HVs. The first HV, named Main<sup>5</sup>, has dimensions of  $480 \times 752 \times 33 \times 31$ , which contains 31 frames, and each frame has 33 bands from 400nm to 720nm wavelength with a 10nm step [81]. We downsample each brand size to  $240 \times 240$  and then reformat the 4D HSV into a  $240 \times 240 \times 33 \times 31$  smaller tensor as a result of computational limitation. The other two HVs<sup>6</sup>, named Oranges1 and Pool5 respectively, both have dimensions of  $200 \times 200 \times 16 \times 200$ .

**Type 5: Face Datasets:** This first face dataset (**Extended YaleFace Dataset B**<sup>7</sup>) includes 38 subjects with 9 poses under 64 illumination conditions [82], [83]. Each face image has the size of  $192 \times 168$ . The image subsets of 38 subjects under 64 illumination with 1 pose are considered as the testing tensor data by formatting the data into a fourth-order tensor with the size of  $192 \times 168 \times 64 \times 38$ .

The second face dataset (**UWA Hyperspectral Face Database**<sup>8</sup>) contains hyperspectral image cubes of 78 subjects imaged in multiple sessions. Each cube includes 33 spectral bands covering the spectral range of 400-720nm with a 10nm step [84]. Each image is cropped (resized) to the size of  $256 \times 256$ . We only select the faces of 30 target objects photographed in 33 bands as our test data, which can be represented by a fourth-order tensor with a size of  $256 \times 256 \times 30 \times 33$ .

**Type 6: Cardiac Magnetic Resonance Images (MRIs):** These datasets are acquired from 33 subjects, each of which consists of 20 frames and 8-15 slices along the long axis [85]. We choose four subjects as the testing cardiac MRIs

(i.e., sol-yxzt-part 1/2/8/30<sup>9</sup>). Each selected subject is a  $256 \times 256 \times 14 \times 20$  or  $256 \times 256 \times 15 \times 20$  tensor whose elements are magnetic resonance imaging measurements indexed by  $(x, y, z, t)$ , where  $(x, y, z)$  is a point in space and  $t$  corresponds to time.

In our experiments, each raw tested tensor is conducted with normalization operation.

**2) Evaluation Metrics:** We employ the mean of peak signal-to-noise ratio (MPSNR), the mean of relative squared error (MRSE), the mean of structural similarity (MSSIM), and the mean of CPU time (MTime) as the quantitative evaluation metric. Meanwhile, the best and the second-best results are highlighted in boldface and blue, respectively. Generally speaking, higher MPSNR/MSSIM values and lower MTime/MRSE indicate better restoration performance.

**3) Relevant Configurations:** In this experiment, we defined the *sampling ratio* (SR) as  $SR = \frac{|\Omega|}{I_1 I_2 \cdots I_N}$  for an  $I_1 \times I_2 \times \cdots \times I_N$  tensor, where the observed index set  $\Omega$  is generated uniformly at random and  $|\Omega|$  represents the cardinality of  $\Omega$ . For robust tensor completion task, the observed tensor is constructed as follows: firstly, sparse pepper-and-salt impulsive noise is added to the underlying tensor with corruption rate  $NR$ <sup>10</sup>, and then incorporate mean-zeros Gaussian noise with a standard deviation of  $\sigma$ . Finally, the observed observations are formed by the given *sampling ratio* SR. The parameters in compared methods are manually adjusted to the optimal performance, which refers to the discussion in their corresponding articles. The parameter settings of the proposed method are detailed in the supplementary material.

## B. Experiment 1: Tensor Completion

**1) Comparison Methods:** We compare the proposed tensor completion method (i.e, FCTN-GNTC) and its two accelerated randomized versions with several state-of-the-art LRTC approaches: TRNNM [34], FCTN-NNM [21], FCTN-TC [20], FCTNFR [51], HTNN [8], METNN [31], WSTNN [28], EMLCP-LRTC [32], OTNN [86], MTTD [30], TCTV-TC [10], GTNN-HOC [41], and t- $\epsilon$ -LogDet [40]. In our randomized versions, one is named R1-FCTN-GNTC, integrating the fixed-rank randomized compression strategy, while the other is called R2-FCTN-GNTC, incorporating the fixed-accuracy randomized compression strategy. To ensure fairness, we configure  $\Phi(\cdot) = \psi(\cdot) = \ell_1$  in the proposed methods.

**2) Results and Analysis:** The quantitative metrics (MPSNR, MSSIM, MRSE, MTime) obtained by the proposed and competitive LRTC methods on different types of tensor datasets are presented in Tables I, II, III. From these comprehensive evaluations, we arrive at the following conclusions: 1) Especially in low-sampling scenarios, compared with previous TR/FCTN-based LRTC methods (e.g., FCTNFR, FCTN-TC, FCTN-NNM, TRNN), the proposed randomized algorithms with jointed **L+S** priors achieve enhanced restoration accuracy while incurring relatively low computational

<sup>1</sup>[https://commons.wikimedia.org/wiki/Google\\_Art\\_Project](https://commons.wikimedia.org/wiki/Google_Art_Project)

<sup>2</sup><https://media.xiph.org/video/derf/>

<sup>3</sup><https://take5.theia.cnes.fr/atdistrib/take5/client/#/home>

<sup>4</sup><https://theia.cnes.fr/atdistrib/rocket/#/home>

<sup>5</sup><https://openremotesensing.net/knowledgebase/hyperspectral-video/>

<sup>6</sup><https://www.hsitracking.com/contest/>

<sup>7</sup><http://vision.ucsd.edu/~iskwak/ExtYaleDatabase/ExtYaleB.html>

<sup>8</sup><https://openremotesensing.net/kb/data/>

<sup>9</sup><https://jtl.lassonde.yorku.ca/software/datasets/>

<sup>10</sup>The Matlab function “imnoise (I, ‘salt & pepper’,  $NR$ )” is used for noise generation, where  $NR$  denotes the normalized noise intensity corresponding to  $\text{SNR} = \frac{1}{NR}$  dB.

TABLE I: Quantitative evaluation PSNR, SSIM, RSE and CPU Time (Second) of various LRTC methods on face datasets.

SR	Evaluation Metric	R1-FCTN -GNTC	R2-FCTN -GNTC	FCTNFR [51]	FCTN-TC [20]	FCTN -NNM [21]	TRNN [34]	TCTV-TC [10]	MTTD [30]	EMLCP -LRTC [32]	WSTNN [28]	METNN [31]	HTNN [8]	OTNN [86]	GTNN -HOC [41]	t- $\epsilon$ -LogDet [40]
0.1%	MPSNR	<b>24.26</b>	<b>24.24</b>	14.58	15.04	18.17	14.33	22.48	16.62	20.24	18.61	14.00	17.92	18.51	18.46	14.18
	MSSIM	<b>0.725</b>	<b>0.732</b>	0.180	0.188	0.612	0.495	0.646	0.592	0.531	0.639	0.440	0.476	0.609	0.355	0.184
	MRSE	<b>0.257</b>	<b>0.257</b>	0.700	0.668	0.523	0.746	<b>0.315</b>	0.583	0.427	0.495	0.763	0.509	0.482	0.472	0.741
	MTime	4578	4872	11244	5009	34357	32969	10198	13091	17061	16782	8484	<b>3489</b>	6905	<b>4523</b>	4796
0.3%	MPSNR	<b>26.95</b>	<b>26.96</b>	19.36	20.28	22.64	20.26	25.21	22.92	23.01	24.21	17.57	22.59	19.96	21.42	16.31
	MSSIM	<b>0.768</b>	<b>0.773</b>	0.367	0.368	0.708	0.667	0.693	0.710	0.500	0.750	0.616	0.599	0.659	0.427	0.244
	MRSE	<b>0.199</b>	<b>0.198</b>	0.429	0.388	0.310	0.403	0.239	0.292	0.311	0.274	0.540	0.294	0.409	0.321	0.586
	MTime	<b>4491</b>	5227	11293	7773	35327	35131	9987	13096	16982	16699	8464	<b>3483</b>	6969	4550	4795
0.5%	MPSNR	<b>28.51</b>	<b>28.58</b>	23.94	24.82	22.44	26.76	25.28	23.66	26.87	20.76	24.70	21.63	22.75	18.00	
	MSSIM	0.788	<b>0.795</b>	0.567	0.527	0.751	0.718	0.713	0.758	0.509	<b>0.797</b>	0.682	0.647	0.700	0.451	0.282
	MRSE	<b>0.172</b>	<b>0.170</b>	0.263	0.264	0.247	0.313	0.205	0.229	0.303	0.208	0.406	0.244	0.342	0.277	0.485
	MTime	5295	5718	11373	9463	34380	35072	10051	13069	16947	16666	8471	<b>3491</b>	7076	<b>4560</b>	4809
1%	MPSNR	<b>31.56</b>	<b>31.60</b>	30.92	28.84	28.21	25.00	29.29	28.45	28.38	29.56	26.49	26.72	24.08	24.63	21.54
	MSSIM	<b>0.836</b>	<b>0.840</b>	0.788	0.696	0.811	0.767	0.755	0.814	0.653	<b>0.836</b>	0.779	0.694	0.751	0.519	0.402
	MRSE	<b>0.123</b>	<b>0.123</b>	<b>0.123</b>	<b>0.157</b>	0.176	0.239	0.158	0.171	0.200	<b>0.157</b>	0.232	0.202	0.263	0.232	0.334
	MTime	6114	6526	11514	11655	34545	33124	10016	12930	17020	16857	8510	<b>3493</b>	7253	<b>4589</b>	4827
3%	MPSNR	<b>36.49</b>	<b>36.47</b>	33.72	33.61	34.04	29.99	33.66	32.57	33.68	34.05	34.90	29.82	28.39	29.33	28.01
	MSSIM	<b>0.915</b>	<b>0.916</b>	0.855	0.836	0.889	0.842	0.825	0.871	0.783	0.889	0.900	0.752	0.828	0.660	0.611
	MRSE	<b>0.066</b>	<b>0.066</b>	<b>0.090</b>	<b>0.090</b>	0.099	0.143	0.103	0.113	0.100	0.099	0.091	0.150	0.168	0.152	0.182
	MTime	8086	8144	8293	13512	34371	31004	10089	11664	17059	16859	8556	<b>3502</b>	7396	<b>4638</b>	4847

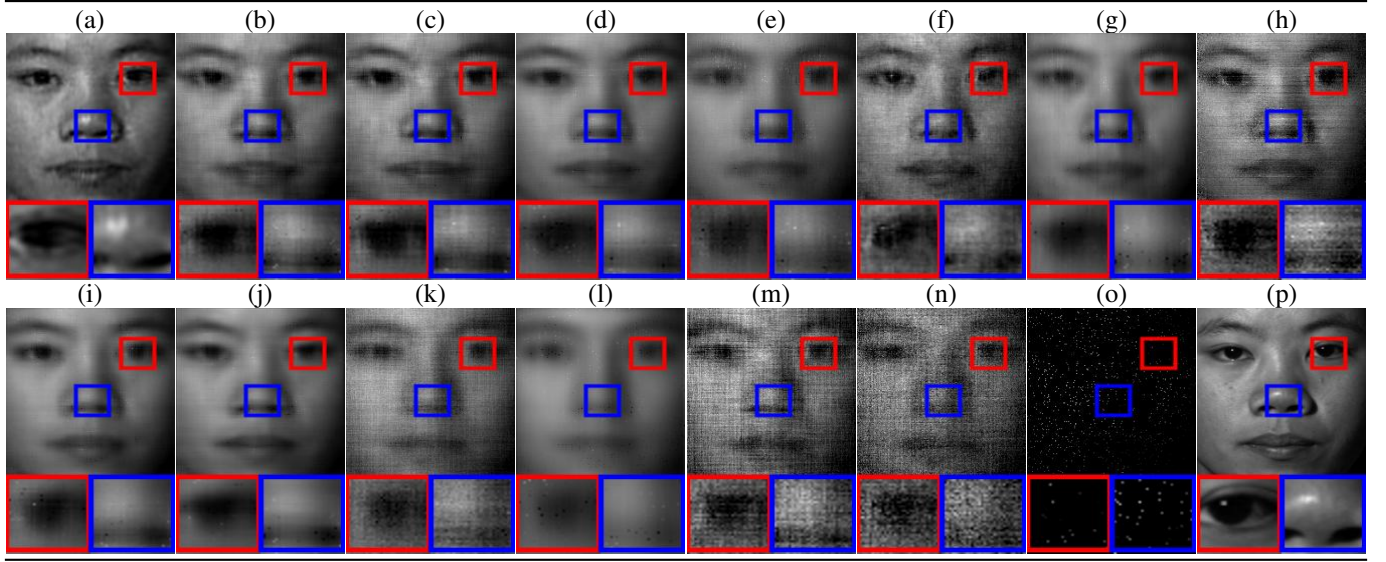
Fig. 1: Visual comparison of various LRTC methods for Face datasets inpainting under  $SR = 1\%$ . From left to right: (a) Ours, (b) FCTNFR, (c) FCTNTC, (d) FCTN-NNM, (e) TRNNM, (f) TCTV, (g) MTTD, (h) EMLCP, (i) WSTNN, (j) METNN, (k) HTNN, (l) OTNN, (m) GTNN-HOC, (n)  $t\text{-}\epsilon\text{-LogDet}$ , (o) Observed, (p) Ground-truth.

TABLE II: Quantitative evaluation PSNR, SSIM, RSE and CPU Time (Second) of various LRTC methods on MRIs.

SR	Evaluation Metric	R1-FCTN -GNTC	R2-FCTN -GNTC	FCTNFR [51]	FCTN-TC [20]	FCTN -NNM [21]	TRNN [34]	TCTV-TC [10]	MTTD [30]	EMLCP -LRTC [32]	WSTNN [28]	METNN [31]	HTNN [8]	OTNN [86]	GTNN -HOC [41]	t- $\epsilon$ -LogDet [40]
0.1%	MPSNR	<b>26.22</b>	<b>27.38</b>	21.14	20.48	19.62	19.19	24.72	21.47	26.21	21.11	19.18	20.89	19.18	21.10	21.31
	MSSIM	0.728	<b>0.780</b>	0.552	0.563	0.577	0.380	<b>0.751</b>	0.678	0.742	0.652	0.335	0.654	0.378	0.469	0.483
	MRSE	<b>0.452</b>	<b>0.398</b>	0.796	0.861	0.952	0.999	0.535	0.776	<b>0.452</b>	0.807	1.000	0.827	0.999	0.791	0.779
	MTime	2008	2264	7238	3974	7087	7974	3948	3987	6150	6462	3198	<b>910</b>	3671	<b>1640</b>	1737
0.3%	MPSNR	<b>28.92</b>	<b>29.91</b>	23.29	21.89	21.81	20.36	27.59	25.79	28.85	23.77	20.85	24.47	22.03	23.88	23.23
	MSSIM	0.777	<b>0.829</b>	0.614	0.574	0.712	0.663	0.789	0.753	<b>0.790</b>	0.732	0.491	0.685	0.675	0.523	0.515
	MRSE	<b>0.333</b>	<b>0.299</b>	0.621	0.732	0.742	0.877	0.388	0.473	0.337	0.599	0.841	0.547	0.730	0.580	0.621
	MTime	2039	2166	7442	4204	6577	8091	3865	4016	6132	6501	3190	<b>945</b>	3798	<b>1675</b>	1765
0.5%	MPSNR	<b>30.72</b>	<b>31.20</b>	25.12	23.21	22.88	21.64	28.83	28.22	<b>30.15</b>	25.67	23.09	26.17	23.32	24.90	24.24
	MSSIM	0.802	<b>0.857</b>	0.665	0.585	0.736	0.716	0.811	<b>0.819</b>	0.816	0.772	0.682	0.717	0.713	0.556	0.536
	MRSE	<b>0.291</b>	<b>0.261</b>	0.502	0.632	0.655	0.757	0.338	0.361	<b>0.291</b>	0.481	0.637	0.452	0.629	0.516	0.559
	MTime	2227	2408	7415	4352	6538	8128	3873	4025	6080	6670	3577	<b>904</b>	3832	<b>1686</b>	1760
1%	MPSNR	31.87	<b>32.06</b>	28.75	25.51	25.21	23.66	30.72	30.66	<b>31.94</b>	29.24	25.77	28.09	25.50	27.35	26.38
	MSSIM	0.834	<b>0.858</b>	0.759	0.638	0.787	0.764	0.843	<b>0.867</b>	0.847	0.838	0.745	0.773	0.766	0.640	0.617
	MRSE	<b>0.241</b>	<b>0.239</b>	0.335	0.486	0.502	0.601	0.272	0.276	<b>0.239</b>	0.322	0.472	0.366	0.491	0.391	0.439
	MTime	2370	2730	7498	4574	7544	8177	4080	4026	6027	8224	3500	<b>948</b>	3875	<b>1703</b>	1769

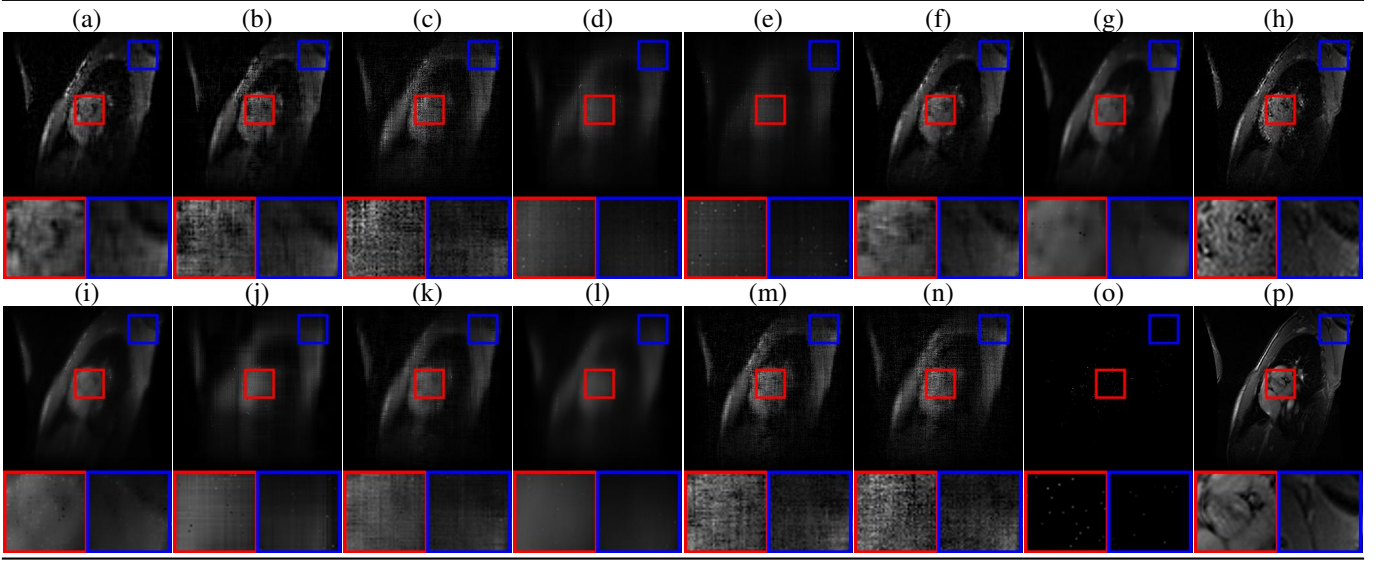


Fig. 2: Visual comparison of various LRTC methods for MRI datasets inpainting under  $SR = 1\%$ . From left to right: (a) Ours, (b) FCTNFR, (c) FCTNTC, (d) FCTN-NNM, (e) TRNNM, (f) TCTV, (g) MTTD, (h) EMLCP, (i) WSTNN, (j) METNN, (k) HTNN, (l) OTNN, (m) GTNN-HOC, (n)  $t\text{-}\epsilon\text{-LogDet}$ , (o) Observed, (p) Ground-truth.

TABLE III: Quantitative evaluation PSNR, SSIM, RSE and CPU Time (Second) of various LRTC methods on MRSIs.

SR	Evaluation Metric	RT-FCTN -GNTC	R2-FCTN -GNTC	FCTNFR [51]	FCTN-TC [20]	FCTN -NNM [21]	TRNN [34]	TCTV-TC [10]	MTTD [30]	EMLCP -LRTC [32]	WSTNN [28]	METNN [31]	HTNN [8]	OTNN [86]	GTNN -HOC [41]	$t\text{-}\epsilon\text{-LogDet}$ [40]
0.5%	MPSNR	<b>21.88</b>	<b>21.84</b>	17.43	17.04	20.63	17.25	21.53	20.95	18.98	20.82	15.77	19.83	19.00	18.32	16.32
	MSSIM	<b>0.537</b>	<b>0.537</b>	0.366	0.368	0.433	0.391	<b>0.536</b>	0.466	0.477	0.470	0.356	0.413	0.409	0.364	0.325
	MRSE	<b>0.301</b>	<b>0.302</b>	0.533	0.556	0.345	0.551	0.316	0.327	0.397	0.349	0.640	0.364	0.462	0.408	0.545
	MTime	<b>2611</b>	3026	14543	10043	11986	13633	9197	9106	19071	20064	9833	<b>2852</b>	5751	3184	3343
1%	MPSNR	<b>23.91</b>	<b>23.70</b>	20.93	19.37	21.54	19.99	23.28	23.02	19.36	22.42	18.41	21.25	20.60	19.75	18.30
	MSSIM	<b>0.658</b>	<b>0.650</b>	0.522	0.462	0.472	0.444	0.639	0.580	0.536	0.563	0.429	0.497	0.462	0.468	0.425
	MRSE	<b>0.234</b>	<b>0.242</b>	0.350	0.416	0.308	0.385	0.256	0.262	0.376	0.287	0.471	0.316	0.367	0.351	0.431
	MTime	<b>2788</b>	3182	15259	12002	12145	13536	9232	8855	19136	20130	9862	<b>2739</b>	5793	3194	3195
3%	MPSNR	26.26	<b>26.27</b>	25.88	23.72	23.64	22.35	<b>26.32</b>	25.52	23.60	24.89	24.03	23.17	23.51	22.11	21.17
	MSSIM	<b>0.791</b>	0.788	0.770	0.718	0.619	0.573	<b>0.794</b>	0.748	0.745	0.716	0.616	0.647	0.646	0.650	0.608
	MRSE	<b>0.185</b>	<b>0.185</b>	0.194	0.248	0.243	0.283	<b>0.183</b>	0.202	0.240	0.202	0.229	0.254	0.259	0.275	0.308
	MTime	3659	4047	22794	18985	12600	16285	10099	8342	17810	18757	12831	<b>2584</b>	6924	3466	<b>3433</b>
5%	MPSNR	<b>27.09</b>	27.06	26.79	25.79	25.02	23.66	<b>27.87</b>	26.85	25.01	26.34	25.49	24.44	24.98	23.75	22.92
	MSSIM	<b>0.831</b>	0.827	0.807	0.786	0.722	0.673	<b>0.850</b>	0.814	0.795	0.788	0.726	0.727	0.736	0.730	0.706
	MRSE	<b>0.171</b>	0.172	0.174	0.199	0.209	0.243	<b>0.157</b>	0.177	0.210	0.177	0.196	0.222	0.220	0.236	0.259
	MTime	4195	4637	23355	19016	12603	16316	11639	7416	17985	15626	12828	<b>2463</b>	6501	3504	<b>3380</b>

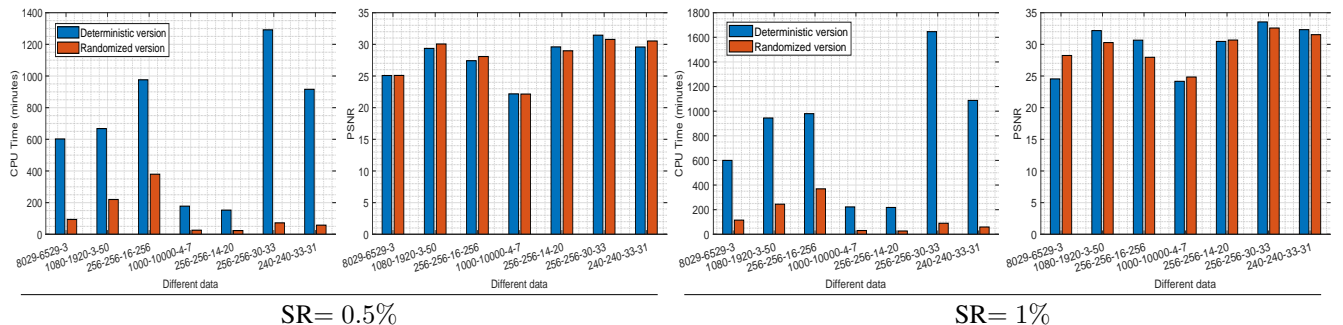


Fig. 3: The tensor data type (from left to right are color image, color video, multi-temporal hyperspectral images, magnetic resonance image, face dataset, hyperspectral video, respectively) versus CPU Time and PSNR in LRTC task. The sampling rates are set to be  $SR = 0.5\%$  and  $SR = 1\%$ , respectively. While maintaining comparable accuracy, the randomized version is on average 9X faster than the deterministic one, and in some individual cases, it achieves up to 20X speedup.

TABLE IV: Quantitative evaluation PSNR, SSIM, RSE, CPU Time (Second) of various RTC methods on MRSIs.

SR & NR	Evaluation Metric	TRNN [35]	TTNN [87]	TSPK [88]	TTLRR [89]	LNOP [42]	NRTRM [43]	HWTNN [90]	HWTSN [9]	R-HWTSN [9]	TCTV-RTC [10]	FCTN -GNRTC	R1-FCTN -GNRTC	R2-FCTN -GNRTC
SR=0.2 & NR=1/3	MPSNR	23.5808	25.0459	25.1370	25.3187	26.1520	25.1798	26.2033	26.5120	26.1580	28.5136	28.4088	<b>28.8936</b>	<b>28.8736</b>
	MSSIM	0.5218	0.6127	0.6151	0.5464	0.6181	0.6340	0.6075	0.6370	0.6177	<b>0.7446</b>	<b>0.7366</b>	0.7365	0.7293
	MRSE	0.2446	0.2315	0.2289	0.2189	0.2041	0.2307	0.1945	0.2000	0.1983	0.1643	0.1510	<b>0.1386</b>	<b>0.1392</b>
	MTIME	3993.67	<b>1524.45</b>	3046.91	3826.11	2484.09	2099.35	2057.09	2684.24	<b>1497.06</b>	4111.31	15397.15	3150.63	3532.49
SR=0.2 & NR=0.5	MPSNR	21.6410	23.3963	23.5539	23.2420	24.1864	23.8436	24.2885	23.7792	23.6564	26.4475	26.4772	<b>27.1675</b>	<b>27.2392</b>
	MSSIM	0.4911	0.4813	0.5010	0.4247	0.5323	0.5515	0.4940	0.5066	0.5090	<b>0.6737</b>	0.6595	<b>0.6704</b>	0.6618
	MRSE	0.3122	0.2677	0.2643	0.2586	0.2523	0.2608	0.2336	0.2594	0.2619	0.2094	0.1871	<b>0.1663</b>	<b>0.1660</b>
	MTIME	4019.17	<b>1569.65</b>	3027.08	3806.64	2601.71	2088.82	2048.02	2673.53	<b>1508.72</b>	3986.73	14095.62	3154.07	3337.86
SR=0.1 & NR=1/3	MPSNR	20.8668	23.5098	23.5289	23.9632	23.8890	23.6531	23.9005	24.0602	23.9741	26.0960	26.1907	<b>26.5446</b>	<b>26.5185</b>
	MSSIM	0.4904	0.5281	0.5283	0.4840	0.4909	0.5482	0.4931	0.5064	0.5002	<b>0.6553</b>	<b>0.6518</b>	0.6494	0.6333
	MRSE	0.3387	0.2711	0.2687	0.2398	0.2518	0.2684	0.2518	0.2473	0.2476	0.2171	0.1999	<b>0.1810</b>	<b>0.1823</b>
	MTIME	3942.03	<b>1719.65</b>	3176.77	3550.68	2213.47	2113.38	1994.28	2654.98	<b>1194.43</b>	4108.24	14158.85	2485.03	2567.18
SR=0.1 & NR=0.5	MPSNR	19.7638	22.1445	22.0155	21.3846	21.8048	22.5362	22.3005	22.1249	22.0964	24.3981	24.2819	<b>24.8372</b>	<b>24.8560</b>
	MSSIM	0.4724	0.4208	0.4306	0.3155	0.4141	0.4767	0.4042	0.3994	0.4069	0.5804	<b>0.5830</b>	<b>0.5915</b>	0.5674
	MRSE	0.3802	0.3121	0.3176	0.2884	0.3380	0.3051	0.3003	0.2963	0.2990	0.2644	0.2576	<b>0.2256</b>	<b>0.2265</b>
	MTIME	3967.29	<b>1731.32</b>	3207.05	3482.18	2268.15	2118.69	1982.68	2636.47	<b>1203.59</b>	4010.51	14412.76	2495.99	2587.71

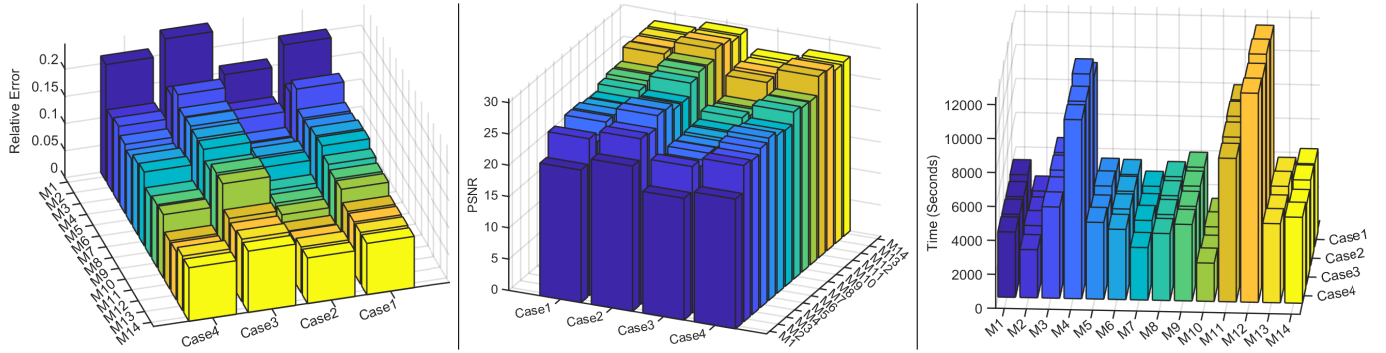


Fig. 4: Quantitative evaluation MPSNR, MSSIM, MRSE and CPU Time (Second) of various RTC methods on four color videos. **X label:** (M1) TRNN, (M2) UTNN, (M3) TSPK, (M4) TTLRR, (M5) LNOP, (M6) NRTRM, (M7) BCNRTC, (M8) HWTNN, (M9) HWTSN, (M10) R-HWTSN, (M11) TCTV-RTC, (M12) FCTN-GNRTC, (M13) R1-FCTN-GNRTC, (M14) R2-FCTN-GNRTC. **Y label:** (Case 1)  $SR = 5\%$ ,  $SNR = 3dB$ , (Case 2)  $SR = 10\%$ ,  $SNR = 3dB$ , (Case 3)  $SR = 5\%$ ,  $SNR = 2dB$ , (Case 4)  $SR = 10\%$ ,  $SNR = 2dB$ .

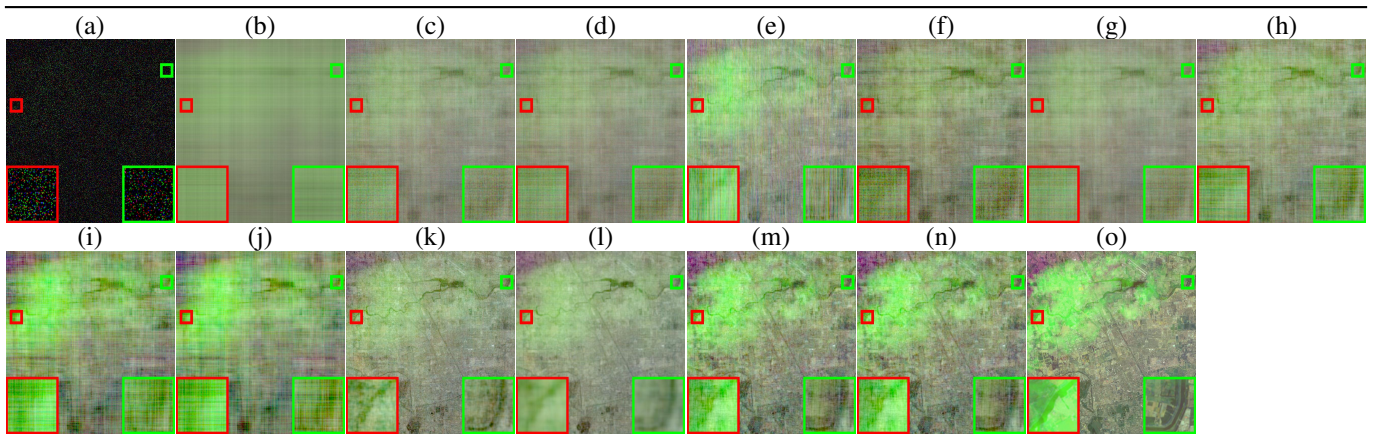


Fig. 5: Visual comparison of various RTC methods for MRSIs inpainting under  $(SR, NR) = (0.1, 0.5)$ . From left to right: (a) Observed, (b) TRNN, (c) TTNN, (d) TSPK, (e) TTLRR, (f) LNOP, (g) NRTRM, (h) HWTNN, (i) HWTSN, (j) R-HWTSN, (k) TCTV-RTC, (l) FCTN-GNRTC, (m) R1-FCTN-GNRTC, (n) R2-FCTN-GNRTC, (o) Ground-truth.

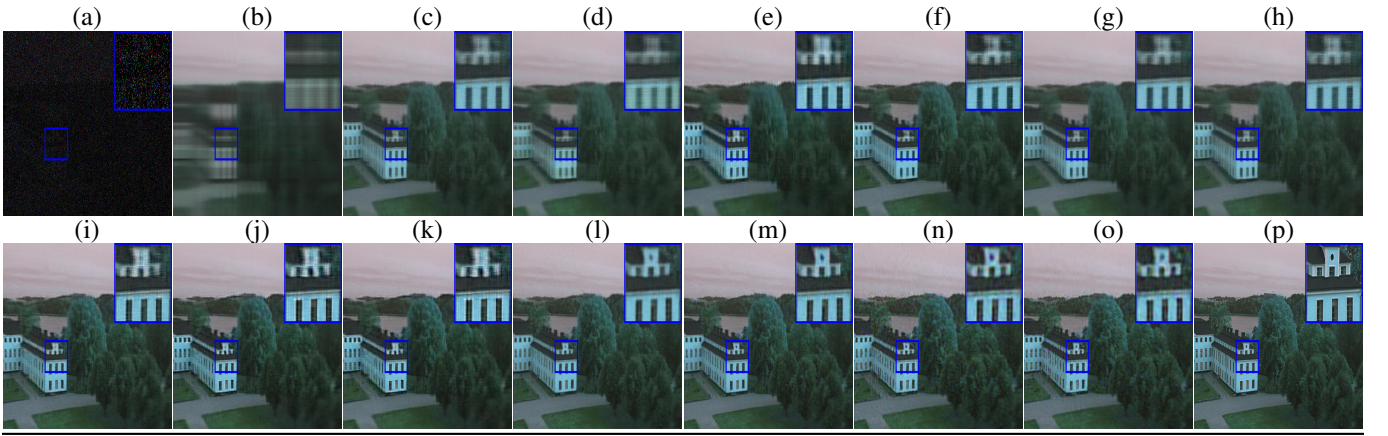


Fig. 6: Visual comparison of various RTC methods for CVs restoration under  $SR = 0.1$ ,  $SNR = 2dB$ . From left to right: (a) Observed, (b) TRNN, (c) TTNN, (d) TSPK, (e) TTLRR, (f) LNOP, (g) NRTRM, (h) BCNRTC, (i) HWTNN, (j) HWTN, (k) R-HWTN, (l) TCTV-RTC, (m) FCTN-GNRTC, (n) R1-FCTN-GNRTC, (o) R2-FCTN-GNRTC, (p) Ground-truth.

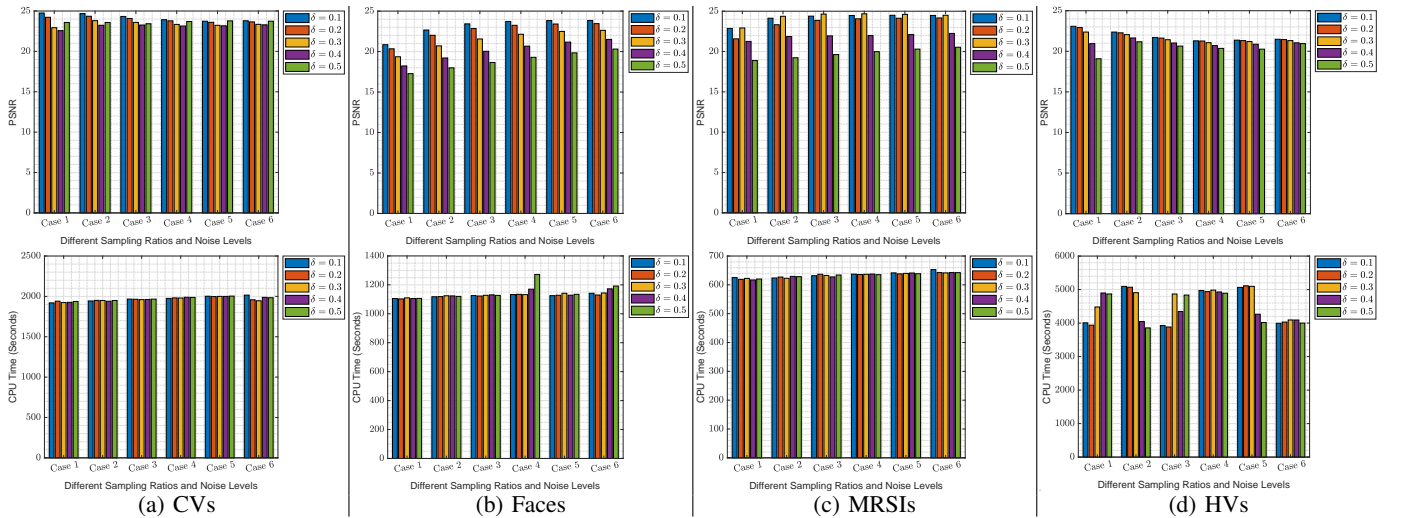


Fig. 7: Recovery performance of the proposed randomized FCTN-GNQRTC on various datasets under different quantization resolutions  $\delta$ , sampling ratios  $SR$ , sparse noise levels  $NR$ , and Gaussian noise levels  $\sigma$ . From left to right are  $SR = 0.1$ ,  $NR = 0.1$ ,  $\sigma = 0.1$  (Case 1),  $SR = 0.2$ ,  $NR = 0.1$ ,  $\sigma = 0.1$  (Case 2),  $SR = 0.3$ ,  $NR = 0.1$ ,  $\sigma = 0.1$  (Case 3),  $SR = 0.4$ ,  $NR = 0.1$ ,  $\sigma = 0.1$  (Case 4),  $SR = 0.5$ ,  $NR = 0.1$ ,  $\sigma = 0.1$  (Case 5) and  $SR = 0.6$ ,  $NR = 0.1$ ,  $\sigma = 0.1$  (Case 6), respectively.

costs; 2) When compared with competitive algorithms (e.g., TCTV-TC, MTTD, EMLCP-LRTC) derived from other tensor frameworks, the proposed method can deliver relatively lower MRSE values, lower CPU runtime in most cases, and higher MPSNR and MSSIM values; 3) Although some methods (e.g., HTNN, GTNN-HOC, t- $\epsilon$ -LogDet) that rely solely on low-rank priors can achieve shorter computation times than the proposed method, they perform significantly worse in terms of various accuracy metrics, namely MPSNR, MSSIM, and MRSE.

The corresponding visual comparisons of locally enlarged regions are exemplified in Figures 1, 2. More visual examples are available in the supplementary materials. From the perspectives of clarity, color richness, texture, and edge information, the proposed method achieves the best visual restoration effect. Especially under extremely low sampling rates, the proposed method is still capable of restoring the

general appearance of visual data, while other comparative algorithms largely fail. Figure 3 illustrates the differences in computational efficiency and recovery accuracy between the randomized and deterministic versions of the proposed method across multiple tensor datasets. We can observe that while maintaining comparable accuracy (measured by PSNR values), the randomized version is on average 9X faster than the deterministic one, and in some individual cases, it achieves up to 20X speedup. As the randomized algorithms induced by the fixed-precision scheme and the fixed-rank strategy achieve similar results, we only present the outcomes of the former.

### C. Experiment 2: Robust Tensor Completion

1) **Comparison Methods:** We compare the proposed method (i.e., FCTN-GNRTC) and its two accelerated randomized versions with several RTC approaches: TRNN [35],

UTNN [87], TSPK [88], TTLRR [89], LNOP [42], NRTRM [43], BCNRTC [44], HWTNN [90], HWTSN [9], R-HWTSN [9], and TCTV-RTC [10]. In our proposed randomized algorithms, the versions coupled with fixed-rank and fixed-accuracy randomized compression strategies are named R1-FCTN-GNRTC and R2-FCTN-GNRTC, respectively. To uphold the principle of fairness, we set both  $\Phi(\cdot)$  and  $\psi(\cdot)$  to be equivalent to the basic  $\ell_1$ -norm in the proposed methods.

2) **Results and Analysis:** Table IV provides a comprehensive comparison of the proposed algorithm against several competitive benchmarks, presenting quantitative results (MPSNR, MSSIM, MRSE, CPU Time) on several MRSI datasets. Figure 4 showcases the corresponding performance outcomes obtained from CV datasets. Accordingly, a comprehensive comparison of the visual quality on two categories of robust completion tasks is illustrated in Figures 5, 6. From these results, we find that in comparison with existing approaches that are only modeled by the global low-rankness prior, the proposed method achieves a  $2 \sim 3$  dB gain in MPSNR. The proposed R1-FCTN-GNRTC and R2-FCTN-GNRTC algorithms reach recovery accuracy similar to the competitive TCTV-RTC algorithm, and at the same time cut down computational time significantly. In the proposed method, the randomized versions are approximately 2.5 times faster than the deterministic version for CVs recovery task, and about 5  $\sim$  7 times faster for MRSIs restoration task.

#### D. Experiment 3: Quantized Tensor Recovery

In this subsection, we firstly focus on investigating the impacts of various quantization resolutions upon the performance of the proposed quantized algorithms under different sampling rates and noise levels. The relevant experimental results are presented in Figures 7, where  $\delta = 0.1, 0.2, 0.3, 0.4, 0.5$ ,  $SR = 0.1, 0.2, 0.3, 0.4, 0.5, 0.6$ ,  $NR = 0.1$ ,  $\sigma = 0.1$ . The results for more sampling and noise corruption scenarios are available in the supplementary materials. From these results, it can be observed that increasing the quantization step size  $\delta$  leads to a gradual decline in recovery performance for the proposed quantized method.

## VII. CONCLUSIONS AND FUTURE WORK

In this article, by investigating efficient gradient-domain regularization and randomized acceleration strategies, we propose a novel scale-aware tensor modeling and computation framework for large-scale high-dimensional visual data recovery. Specifically, we put forward reliable and effective tensor models by an innovative gradient-domain regularization scheme based on FCTN decomposition, where the observation transitions from non-quantized scenarios to quantized scenarios. To alleviate the computational bottlenecks encountered in processing large-scale data, fast randomized compression and representation strategies are developed as the core acceleration modules in algorithm design. From a theoretical perspective, the theoretical error bounds and convergence properties of the proposed algorithms are analyzed. Extensive experimental results on various multi-dimensional tensor datasets have demonstrated the effectiveness and superiority of the proposed

method compared to current competing approaches. In future work, by integrating tensor methods/theories, quantization, randomized sketching with deep-learning techniques, we plan to research faster and more efficient approaches for large-scale high-dimensional data approximation and recovery.

## REFERENCES

- [1] R. Han, R. Willett, and A. R. Zhang, “An optimal statistical and computational framework for generalized tensor estimation,” *Ann. Statist.*, vol. 50, no. 1, pp. 1–29, 2022.
- [2] J.-F. Cai, J. Li, and D. Xia, “Generalized low-rank plus sparse tensor estimation by fast riemannian optimization,” *J. Am. Stat. Assoc.*, vol. 118, no. 544, pp. 2588–2604, 2023.
- [3] A. G. Mahyari, D. M. Zoltowski *et al.*, “A tensor decomposition-based approach for detecting dynamic network states from EEG,” *IEEE Trans. Biomed. Eng.*, vol. 64, no. 1, pp. 225–237, 2016.
- [4] C. Liu, S. Li, D. Hu, J. Wang, W. Qin, C. Liu, and P. Zhang, “Nonlocal tensor decomposition with joint low rankness and smoothness for spectral CT image reconstruction,” *IEEE Trans. Comput. Imag.*, vol. 10, pp. 613–627, 2024.
- [5] D. Wang, M. Hu, Y. Jin, Y. Miao, J. Yang, Y. Xu, X. Qin, J. Ma, L. Sun, C. Li *et al.*, “Hypersigma: Hyperspectral intelligence comprehension foundation model,” *IEEE Trans. Pattern Anal. Mach. Intell.*, vol. 47, no. 8, pp. 6427–6444, 2025.
- [6] W. Qin, H. Wang, F. Zhang, J. Wang, X. Cao, and X.-L. Zhao, “Tensor ring decomposition-based generalized and efficient nonconvex approach for hyperspectral anomaly detection,” *IEEE Trans. Geosci. Remote Sens.*, vol. 62, 2024, Art. no. 5539818.
- [7] W. Qin, H. Wang, H. Shu, F. Zhang, J. Wang, X. Cao, X.-L. Zhao, and G. Vivone, “Hyperspectral anomaly detection fused unified nonconvex tensor ring factors regularization,” *IEEE Trans. Geosci. Remote Sens.*, vol. 63, 2025, Art. no. 5533521.
- [8] W. Qin, H. Wang, F. Zhang, J. Wang, X. Luo, and T. Huang, “Low-rank high-order tensor completion with applications in visual data,” *IEEE Trans. Image Process.*, vol. 31, pp. 2433–2448, 2022.
- [9] W. Qin, H. Wang, F. Zhang, W. Ma, J. Wang, and T. Huang, “Non-convex robust high-order tensor completion using randomized low-rank approximation,” *IEEE Trans. Image Process.*, vol. 33, pp. 2835–2850, 2024.
- [10] H. Wang, J. Peng, W. Qin, J. Wang, and D. Meng, “Guaranteed tensor recovery fused low-rankness and smoothness,” *IEEE Trans. Pattern Anal. Mach. Intell.*, vol. 45, no. 9, pp. 10990–11007, 2023.
- [11] Y. Luo, X. Zhao, Z. Li, M. K. Ng, and D. Meng, “Low-rank tensor function representation for multi-dimensional data recovery,” *IEEE Trans. Pattern Anal. Mach. Intell.*, vol. 46, no. 5, pp. 3351–3369, 2024.
- [12] A. Cichocki, N. Lee, I. Oseledets, A.-H. Phan, Q. Zhao, D. P. Mandic *et al.*, “Tensor networks for dimensionality reduction and large-scale optimization: Part 1 low-rank tensor decompositions,” *Found. Trends Mach. Learn.*, vol. 9, no. 4–5, pp. 249–429, 2016.
- [13] N. Park, B. Jeon, J. Lee, and U. Kang, “Bigtensor: Mining billion-scale tensor made easy,” in *Proceedings of the 25th ACM International on Conference on Information and Knowledge Management*, 2016, pp. 2457–2460.
- [14] Q. Song, H. Ge, J. Caverlee, and X. Hu, “Tensor completion algorithms in big data analytics,” *ACM Trans. Knowl. Discov. Data (TKDD)*, vol. 13, no. 1, pp. 1–48, 2019.
- [15] Y. Liu, *Tensors for data processing: theory, methods, and applications*. Academic Press, 2021.
- [16] Y. Liu, J. Liu, Z. Long, and C. Zhu, *Tensor computation for data analysis*. Springer, 2022.
- [17] T. Tong, C. Ma, A. Prater-Bennette, E. Tripp, and Y. Chi, “Scaling and scalability: Provable nonconvex low-rank tensor estimation from incomplete measurements,” *J. Mach. Learn. Res.*, vol. 23, no. 163, pp. 1–77, 2022.
- [18] Z. Qin, M. B. Wakin, and Z. Zhu, “Guaranteed nonconvex factorization approach for tensor train recovery,” *J. Mach. Learn. Res.*, vol. 25, no. 383, pp. 1–48, 2024.
- [19] X. P. Li, Z.-Y. Wang, Z.-L. Shi, H. C. So, and N. D. Sidiropoulos, “Robust tensor completion via capped frobenius norm,” *IEEE Trans. Neural Netw. Learn. Syst.*, vol. 35, no. 7, pp. 9700–9712, 2024.
- [20] Y.-B. Zheng, T.-Z. Huang, X.-L. Zhao, Q. Zhao, and T.-X. Jiang, “Fully-connected tensor network decomposition and its application to higher-order tensor completion,” in *Proc. AAAI Conf. Artifi. Intell.*, vol. 35, no. 12, 2021, pp. 11 071–11 078.

[21] Y.-Y. Liu, X.-L. Zhao, G.-J. Song, Y.-B. Zheng, M. K. Ng, and T.-Z. Huang, “Fully-connected tensor network decomposition for robust tensor completion problem,” *Inverse Probl. Imag.*, vol. 18, no. 1, pp. 208–238, 2024.

[22] Z.-C. Wu, T.-Z. Huang, L.-J. Deng, H.-X. Dou, and D. Meng, “Tensor wheel decomposition and its tensor completion application,” in *Proc. Adv. Neural Inf. Process. Syst. (NIPS)*, vol. 35, pp. 27 008–27 020, 2022.

[23] Z. Liu, Z. Han, Y. Tang, X.-L. Zhao, and Y. Wang, “Low-tubal-rank tensor recovery via factorized gradient descent,” *IEEE Trans. Signal Process.*, vol. 72, pp. 5470–5483, 2024.

[24] J. Liu, P. Musialski, P. Wonka, and J. Ye, “Tensor completion for estimating missing values in visual data,” *IEEE Trans. Pattern Anal. Mach. Intell.*, vol. 35, no. 1, pp. 208–220, 2012.

[25] D. Goldfarb and Z. Qin, “Robust low-rank tensor recovery: Models and algorithms,” *SIAM J. Matrix Anal. Appl.*, vol. 35, no. 1, pp. 225–253, 2014.

[26] B. Huang, C. Mu *et al.*, “Provable models for robust low-rank tensor completion,” *Pac. J. Optim.*, vol. 11, no. 2, pp. 339–364, 2015.

[27] C. Mu, B. Huang, J. Wright, and D. Goldfarb, “Square deal: Lower bounds and improved relaxations for tensor recovery,” in *Proc. 31st Int. Conf. Mach. Learn. (ICML)*, 2014, pp. 73–81.

[28] Y.-B. Zheng, T.-Z. Huang, X.-L. Zhao, T.-X. Jiang, T.-Y. Ji, and T.-H. Ma, “Tensor n-tubal rank and its convex relaxation for low-rank tensor recovery,” *Inf. Sci.*, vol. 532, pp. 170–189, 2020.

[29] A. Wang, C. Li, Z. Jin, and Q. Zhao, “Robust tensor decomposition via orientation invariant tubal nuclear norms,” in *Proc. AAAI Conf. Artif. Intell.*, vol. 34, no. 04, 2020, pp. 6102–6109.

[30] L. Feng, C. Zhu, Z. Long, J. Liu, and Y. Liu, “Multiplex transformed tensor decomposition for multidimensional image recovery,” *IEEE Trans. Image Process.*, vol. 32, pp. 3397–3412, 2023.

[31] S. Liu, X.-L. Zhao, J. Leng, B.-Z. Li, J.-H. Yang, and X. Chen, “Revisiting high-order tensor singular value decomposition from basic element perspective,” *IEEE Trans. Signal Process.*, vol. 72, pp. 4589–4603, 2024.

[32] H. Zhang, X. Liu, C. Liu, H. Fan, Y. Li, and X. Zhu, “Tensor recovery based on a novel non-convex function minimax logarithmic concave penalty function,” *IEEE Trans. Image Process.*, vol. 32, pp. 3413–3428, 2023.

[33] J. A. Benua, H. N. Phien, H. D. Tuan, and M. N. Do, “Efficient tensor completion for color image and video recovery: Low-rank tensor train,” *IEEE Trans. Image Process.*, vol. 26, no. 5, pp. 2466–2479, 2017.

[34] J. Yu, C. Li, Q. Zhao, and G. Zhao, “Tensor-ring nuclear norm minimization and application for visual: Data completion,” in *IEEE Int. Conf. Acoust., Speech Signal Process. (ICASSP)*, 2019, pp. 3142–3146.

[35] H. Huang, Y. Liu, Z. Long, and C. Zhu, “Robust low-rank tensor ring completion,” *IEEE Trans. Comput. Imag.*, vol. 6, pp. 1117–1126, 2020.

[36] L. Yuan, C. Li, D. Mandic, J. Cao, and Q. Zhao, “Tensor ring decomposition with rank minimization on latent space: An efficient approach for tensor completion,” in *Proc. AAAI Conf. Artif. Intell.*, vol. 33, 2019, pp. 9151–9158.

[37] X. Zhang, “A nonconvex relaxation approach to low-rank tensor completion,” *IEEE Transactions on Neural Networks and Learning Systems*, vol. 30, no. 6, pp. 1659–1671, 2018.

[38] X. Zhang, D. Wang, Z. Zhou, and Y. Ma, “Robust low-rank tensor recovery with rectification and alignment,” *IEEE Trans. Pattern Anal. Mach. Intell.*, vol. 43, no. 1, pp. 238–255, 2019.

[39] H. Wang, F. Zhang, J. Wang, T. Huang *et al.*, “Generalized nonconvex approach for low-tubal-rank tensor recovery,” *IEEE Trans. Neural Netw. Learn. Syst.*, vol. 33, no. 8, pp. 3305–3319, 2021.

[40] M. Yang, Q. Luo, W. Li, and M. Xiao, “3-d array image data completion by tensor decomposition and nonconvex regularization approach,” *IEEE Trans. Signal Process.*, vol. 70, pp. 4291–4304, 2022.

[41] Z.-Y. Wang, H. C. So, and A. M. Zoubir, “Low-rank tensor completion via novel sparsity-inducing regularizers,” *IEEE Trans. Signal Process.*, vol. 72, pp. 3519–3534, 2024.

[42] L. Chen, X. Jiang, X. Liu, and Z. Zhou, “Robust low-rank tensor recovery via nonconvex singular value minimization,” *IEEE Trans. Image Process.*, vol. 29, pp. 9044–9059, 2020.

[43] D. Qiu, M. Bai *et al.*, “Nonlocal robust tensor recovery with nonconvex regularization,” *Inverse Probl.*, vol. 37, no. 3, p. 035001, 2021.

[44] X. Zhao, M. Bai, D. Sun, and L. Zheng, “Robust tensor completion: Equivalent surrogates, error bounds, and algorithms,” *SIAM J. Imaging Sci.*, vol. 15, no. 2, pp. 625–669, 2022.

[45] D. Qiu, B. Yang, and X. Zhang, “Robust tensor completion via dictionary learning and generalized nonconvex regularization for visual data recovery,” *IEEE Trans. Circuits Syst. Video Technol.*, 2024.

[46] K. Gao and Z.-H. Huang, “Tensor robust principal component analysis via tensor fibered rank and  $\ell_p$  minimization,” *SIAM J. Imaging Sci.*, vol. 16, no. 1, pp. 423–460, 2023.

[47] Q. Yu and M. Bai, “Generalized nonconvex hyperspectral anomaly detection via background representation learning with dictionary constraint,” *SIAM J. Imag. Sci.*, vol. 17, no. 2, pp. 917–950, 2024.

[48] J. Hou, X. Liu, H. Wang, and K. Guo, “Tensor recovery from binary measurements fused low-rankness and smoothness,” *Signal Process.*, vol. 221, p. 109480, 2024.

[49] Y. Zhang, Z. Tu, J. Lu, C. Xu, and L. Shen, “Fusion of low-rankness and smoothness under learnable nonlinear transformation for tensor completion,” *Knowl.-Based Syst.*, vol. 296, p. 111917, 2024.

[50] Q. Feng, J. Hou, W. Kong, C. Xu, and J. Wang, “Poisson tensor completion with transformed correlated total variation regularization,” *Pattern Recognit.*, vol. 156, p. 110735, 2024.

[51] Y.-B. Zheng, T.-Z. Huang, X.-L. Zhao, and Q. Zhao, “Tensor completion via fully-connected tensor network decomposition with regularized factors,” *J. Sci. Comput.*, vol. 92, no. 1, p. 8, 2022.

[52] C.-Y. Lyu, X.-L. Zhao, B.-Z. Li, H. Zhang, and T.-Z. Huang, “Multi-dimensional image recovery via fully-connected tensor network decomposition under the learnable transforms,” *J. Sci. Comput.*, vol. 93, no. 2, p. 49, 2022.

[53] W.-J. Zheng, X.-L. Zhao, Y.-B. Zheng, J. Lin, L. Zhuang, and T.-Z. Huang, “Spatial-spectral-temporal connective tensor network decomposition for thick cloud removal,” *ISPRS J. Photogramm. Remote Sens.*, vol. 199, pp. 182–194, 2023.

[54] Z. Tu, J. Lu, H. Zhu, W. Hu, Q. Jiang, and M. K. Ng, “Fully-connected tensor network decomposition and group sparsity for multitemporal images cloud removal,” *Inverse Probl. Imag.*, 2024.

[55] J. Yu, Z. Li, G. Ma, J. Wang, T. Zou, and G. Zhou, “Low-rank sparse fully-connected tensor network for tensor completion,” *Pattern Recognit.*, vol. 158, p. 111000, 2025.

[56] Z.-L. Han, T.-Z. Huang, X.-L. Zhao, H. Zhang, and W.-H. Wu, “Nested fully-connected tensor network decomposition for multi-dimensional visual data recovery,” *IEEE Trans. Circuits Syst. Video Technol.*, 2024.

[57] W.-J. Zheng, X.-L. Zhao, Y.-B. Zheng, and T.-Z. Huang, “Provable stochastic algorithm for large-scale fully-connected tensor network decomposition,” *J. Sci. Comput.*, vol. 98, no. 1, p. 16, 2024.

[58] J. Chen, C.-L. Wang, M. K. Ng, and D. Wang, “High dimensional statistical estimation under uniformly dithered one-bit quantization,” *IEEE Trans. Inf. Theory*, vol. 69, no. 8, pp. 5151–5187, 2023.

[59] J. Hou, F. Zhang, H. Qiu, J. Wang, Y. Wang, and D. Meng, “Robust low-tubal-rank tensor recovery from binary measurements,” *IEEE Trans. Pattern Anal. Mach. Intell.*, vol. 44, no. 8, pp. 4355–4373, 2021.

[60] J. Hou, J. Chen, and M. K. Ng, “Robust tensor completion from uniformly dithered one-bit observations,” *SIAM J. Imag. Sci.*, vol. 18, no. 1, pp. 152–215, 2025.

[61] R. Minster, A. K. Saibaba, and M. E. Kilmer, “Randomized algorithms for low-rank tensor decompositions in the tucker format,” *SIAM J. Math. Data Sci.*, vol. 2, no. 1, pp. 189–215, 2020.

[62] M. Che, Y. Wei, and H. Yan, “Efficient randomized algorithms for fixed precision problem of approximate tucker decomposition,” *SIAM J. Matrix Anal. Appl.*, vol. 46, no. 1, pp. 256–297, 2025.

[63] M. Wang, Y. Yu, and H. Li, “Randomized tensor wheel decomposition,” *SIAM J. Sci. Comput.*, vol. 46, no. 3, pp. A1714–A1746, 2024.

[64] J. Chen, Y. Wang, and M. K. Ng, “Quantized low-rank multivariate regression with random dithering,” *IEEE Trans. Signal Process.*, vol. 71, pp. 3913–3928, 2023.

[65] Y. He, X. Liu, B. Zheng, J. Hou, and J. Wang, “Robust hyperspectral image recovery from low-resolution quantized incomplete observations,” *Digital Signal Processing*, p. 105371, 2025.

[66] J. Hou and M. K. Ng, “Tensor recovery from quantized measurements based on mode-wise operators,” *Information and Inference: A Journal of the IMA*, vol. 14, no. 2, p. iiaf016, 2025.

[67] T. G. Kolda and B. W. Bader, “Tensor decompositions and applications,” *SIAM Rev.*, vol. 51, no. 3, pp. 455–500, 2009.

[68] N. Vannieuwenhoven, R. Vandebril, and K. Meerbergen, “A new truncation strategy for the higher-order singular value decomposition,” *SIAM J. Sci. Comput.*, vol. 34, no. 2, pp. A1027–A1052, 2012.

[69] W. Dong, G. Yu, L. Qi, and X. Cai, “Practical sketching algorithms for low-rank tucker approximation of large tensors,” *J. Sci. Comput.*, vol. 95, no. 2, p. 52, 2023.

[70] W. Yu, Y. Gu, and Y. Li, “Efficient randomized algorithms for the fixed-precision low-rank matrix approximation,” *SIAM J. Matrix Anal. Appl.*, vol. 39, no. 3, pp. 1339–1359, 2018.

[71] X. Feng and W. Yu, “A fast adaptive randomized PCA algorithm.” in *IJCAI*, 2023, pp. 3695–3704.

- [72] X. Feng, W. Yu, Y. Xie, and J. Tang, “Algorithm 1043: Faster randomized SVD with dynamic shifts,” *ACM Transactions on Mathematical Software*, vol. 50, no. 2, pp. 1–27, 2024.
- [73] H.-Y. Gao and A. G. Bruce, “Waveshrink with firm shrinkage,” *Statistica Sinica*, pp. 855–874, 1997.
- [74] P. Gong, C. Zhang, Z. Lu, J. Huang, and J. Ye, “A general iterative shrinkage and thresholding algorithm for non-convex regularized optimization problems,” in *Proc. Int. Conf. Mach. Learn. (ICML)*. PMLR, 2013, pp. 37–45.
- [75] G. Marjanovic and V. Solo, “On  $\ell_q$  optimization and matrix completion,” *IEEE Trans. Signal Process.*, vol. 60, no. 11, pp. 5714–5724, 2012.
- [76] G. Li, G. Guo, S. Peng, C. Wang, S. Yu, J. Niu, and J. Mo, “Matrix completion via schatten capped  $p$  norm,” *IEEE Trans. Knowl. Data Eng.*, vol. 34, no. 1, pp. 394–404, 2020.
- [77] L. Pan and X. Chen, “Group sparse optimization for images recovery using capped folded concave functions,” *SIAM J. Imag. Sci.*, vol. 14, no. 1, pp. 1–25, 2021.
- [78] J. Fan and R. Li, “Variable selection via nonconcave penalized likelihood and its oracle properties,” *J. Amer. Statist. Assoc.*, vol. 96, no. 456, pp. 1348–1360, 2001.
- [79] C.-H. Zhang, “Nearly unbiased variable selection under minimax concave penalty,” *Ann. Statist.*, vol. 38, no. 2, pp. 894–942, 2010.
- [80] S. Boyd, N. Parikh, E. Chu *et al.*, “Distributed optimization and statistical learning via the alternating direction method of multipliers,” *Found. Trends Mach. Learn.*, vol. 3, no. 1, pp. 1–122, 2011.
- [81] A. Mian and R. Hartley, “Hyperspectral video restoration using optical flow and sparse coding,” *Opt. Express*, vol. 20, no. 10, pp. 10658–10673, 2012.
- [82] A. S. Georghiades, P. N. Belhumeur, and D. J. Kriegman, “From few to many: Illumination cone models for face recognition under variable lighting and pose,” *IEEE Trans. Pattern Anal. Mach. Intell.*, vol. 23, no. 6, pp. 643–660, 2001.
- [83] K.-C. Lee, J. Ho, and D. J. Kriegman, “Acquiring linear subspaces for face recognition under variable lighting,” *IEEE Trans. Pattern Anal. Mach. Intell.*, vol. 27, no. 5, pp. 684–698, 2005.
- [84] M. Uzair, A. Mahmood, and A. Mian, “Hyperspectral face recognition with spatiotemporal information fusion and PLS regression,” *IEEE Trans. Image Process.*, vol. 24, no. 3, pp. 1127–1137, 2015.
- [85] A. Andreopoulos and J. K. Tsotsos, “Efficient and generalizable statistical models of shape and appearance for analysis of cardiac MRI,” *Medical image analysis*, vol. 12, no. 3, pp. 335–357, 2008.
- [86] Y. Qiu, G. Zhou, A. Wang, Q. Zhao, and S. Xie, “Balanced unfolding induced tensor nuclear norms for high-order tensor completion,” *IEEE Trans. Neural Netw. Learn. Syst.*, vol. 36, no. 3, pp. 4724–4737, 2025.
- [87] G. Song, M. K. Ng, and X. Zhang, “Robust tensor completion using transformed tensor singular value decomposition,” *Numer. Linear Algebr. Appl.*, vol. 27, no. 3, p. e2299, 2020.
- [88] J. Lou and Y.-M. Cheung, “Robust low-rank tensor minimization via a new tensor spectral  $k$ -support norm,” *IEEE Trans. Image Process.*, vol. 29, pp. 2314–2327, 2019.
- [89] J.-H. Yang, C. Chen, H.-N. Dai, M. Ding, Z.-B. Wu, and Z. Zheng, “Robust corrupted data recovery and clustering via generalized transformed tensor low-rank representation,” *IEEE Trans. Neural Netw. Learn. Syst.*, vol. 35, no. 7, pp. 8839–8853, 2024.
- [90] W. Qin, H. Wang, F. Zhang, M. Dai, and J. Wang, “Robust low-rank tensor reconstruction using high-order t-SVD,” *J. Electron. Imag.*, vol. 30, no. 6, pp. 063016–063016, 2021.